SPECIAL
TRMM Diabatic Heating
COLLECTION

Observed Large-Scale Structures and Diabatic Heating and Drying Profiles during TWP-ICE

SHAOCHENG XIE

Lawrence Livermore National Laboratory, Livermore, California

TIMOTHY HUME

Centre for Australian Weather and Climate Research, Melbourne, Victoria, Australia

CHRISTIAN JAKOB

School of Mathematical Sciences, Monash University, Melbourne, Victoria, Australia

STEPHEN A. KLEIN AND RENATA B. MCCOY

Lawrence Livermore National Laboratory, Livermore, California

MINGHUA ZHANG

School of Marine and Atmospheric Sciences, Stony Brook University, Stony Brook, New York

ABSTRACT

This study documents the characteristics of the large-scale structures and diabatic heating and drying profiles observed during the Tropical Warm Pool–International Cloud Experiment (TWP-ICE), which was conducted in January–February 2006 in Darwin during the northern Australian monsoon season. The examined profiles exhibit significant variations between four distinct synoptic regimes that were observed during the experiment. The active monsoon period is characterized by strong upward motion and large advective cooling and moistening throughout the entire troposphere, while the suppressed and clear periods are dominated by moderate midlevel subsidence and significant low- to midlevel drying through horizontal advection. The midlevel subsidence and horizontal dry advection are largely responsible for the dry midtroposphere observed during the suppressed period and limit the growth of clouds to low levels. During the break period, upward motion and advective cooling and moistening located primarily at midlevels dominate together with weak advective warming and drying (mainly from horizontal advection) at low levels. The variations of the diabatic heating and drying profiles with the different regimes are closely associated with differences in the large-scale structures, cloud types, and rainfall rates between the regimes. Strong diabatic heating and drying are seen throughout the troposphere during the active monsoon period while they are moderate and only occur above 700 hPa during the break period. The diabatic heating and drying tend to have their maxima at low levels during the suppressed periods. The diurnal variations of these structures between monsoon systems, continental/coastal, and tropical inland-initiated convective systems are also examined.

1. Introduction

The large-scale state of the tropical atmosphere as characterized by low-level convergence and advective cooling and moistening plays an important role in destabilizing the atmospheric structure, initiating and maintaining deep convection. On the other hand, latent heating released from tropical convective systems is a major energy source for the large-scale circulation. By releasing latent heat and vertically redistributing sensible heat and water vapor, cumulus clouds modify the temperature and moisture structure of the environment

Corresponding author address: Shaocheng Xie, Lawrence Livermore National Laboratory, P.O. Box 808, Livermore, CA 94551-0808.
E-mail: xie2@llnl.gov

(Riehl and Malkus 1958; Yanai 1961; Yanai and Johnson 1993). Documenting the large-scale structure and latent heating profiles of tropical convective cloud systems from observations is a key step toward understanding how cumulus convection interacts with its large-scale environment. This has been one of the primary goals of a number of major field experiments conducted in the tropics (Thompson et al. 1979; Frank 1978; Frank and McBride 1989; Lin and Johnson 1996a,b; Schumacher et al. 2007). Retrieval of latent heating profiles from satellite measurements is also a major research topic of the National Aeronautics and Space Administration's (NASA) Tropical Rainfall Measuring Mission (TRMM) (Tao et al. 2006, 2007).

Latent heating is the dominant component of total diabatic heating in the tropics during convective periods. The total diabatic heating and drying can be estimated as the residuals of heat and moisture budgets of large-scale motion measured by a suitably designed sounding network. The purpose of this study is to document the characteristics of the large-scale structure and diabatic heating and drying profiles of the convective cloud systems observed during the latest major field experiment in the tropics, the Tropical Warm Pool–International Cloud Experiment (TWP-ICE). The derived diabatic heating data can also be used as an observed base for validating TRMM latent heating retrievals, which are designed for application with satellite-estimated surface rain rate and precipitation profile inputs using physically based models, which range from simple profile shapes to cloud-resolving models (CRMs). As shown in Tao et al. (2006), different retrieval algorithms may result in large differences in the retrieved latent heating profiles from TRMM measurements.

TWP-ICE was conducted in January–February 2006 in Darwin during the northern Australian monsoon season by the U.S. Department of Energy (DOE) Atmospheric Radiation Measurement Program (ARM) (Stokes and Schwartz 1994; Ackerman and Stokes 2003) and the Australian Bureau of Meteorology (BOM) in collaboration with many other agencies and universities (May et al. 2008) to further improve the understanding of the interaction of tropical convection with its environment. The major goal of TWP-ICE was to provide a comprehensive dataset that describes the structure and evolution of monsoonal deep tropical convection and the resulting cirrus clouds and their radiative impacts. In conjunction with the description of the convection, the experiment aimed to provide an extensive description of the large-scale state of the atmosphere on the scale of a typical climate model grid box ($\sim 2° \times 2°$). For this purpose, a comprehensive ground-based observational network, including an array of six radiosonde stations centered at the ARM Darwin site and an extensive set of in situ and remote sensing instruments, was deployed to observe the evolution of convective cloud systems, their large-scale environment, and the detailed cloud microphysical properties (Fig. 1). One of the unique features of TWP-ICE is that radiosondes were launched with very high temporal resolution (3-hourly launches) at all of the five boundary sounding stations. Consequently, the diurnal variability of convective cloud systems can be better resolved by TWP-ICE data than in data from earlier tropical field experiments.

The northern Australian summer monsoon season usually begins in mid- to late December and ends in March. Climatologically, the monsoonal flow is characterized by low-level westerlies of equatorial origin overlain by strong easterlies in the upper troposphere, with "break" periods where low- to midlevel easterlies of continental origin prevail. Characteristics of the convection and its associated large-scale environment during the northern Australian summer monsoon season have been described in many studies. An overview of the northern Australian summer monsoon was provided by McBride (1987) and Manton and McBride (1992); Gunn et al. (1989) described the synoptic aspects of the 1987 Australian summer monsoon during the Australian Monsoon Experiment (AMEX) over the Gulf of Carpentaria; Frank and McBride (1989) performed a detailed investigation of diabatic heating and drying structures and the evolution of the life cycle of the convective cloud systems for AMEX. They found that AMEX convective systems typically showed stronger upward motion and more heating in the mid- and upper levels but weaker upward motion and less heating in the lower troposphere throughout their life cycles compared to those systems observed in Atlantic Ocean during the Global Atmospheric Research Program (GARP) Atlantic Tropical Experiment (GATE). Keenan and Carbone (1992) showed differences in the structural characteristics of tropical precipitating systems of oceanic, continental/coastal, and island origin observed in the vicinity of Darwin. Tropical island-initiated convective systems over the Darwin region were studied in Carbone et al. (2000) and were the major focus of the Maritime Continent Thunderstorm Experiment (MCTEX) held during November–December 1995 over the Tiwi Islands north of Darwin (Keenan et al. 2000).

During TWP-ICE, Darwin experienced four distinct synoptic regimes, coincident with the activity of a major Madden–Julian oscillation (MJO) event that influenced the region (see the MJO index online at http://www.bom.gov.au/bmrc/clfor/cfstaff/matw/maproom/RMM/). Various types of tropical convective systems of oceanic, continental/coastal, and island origin were observed during the experiment. The experiment provided a unique
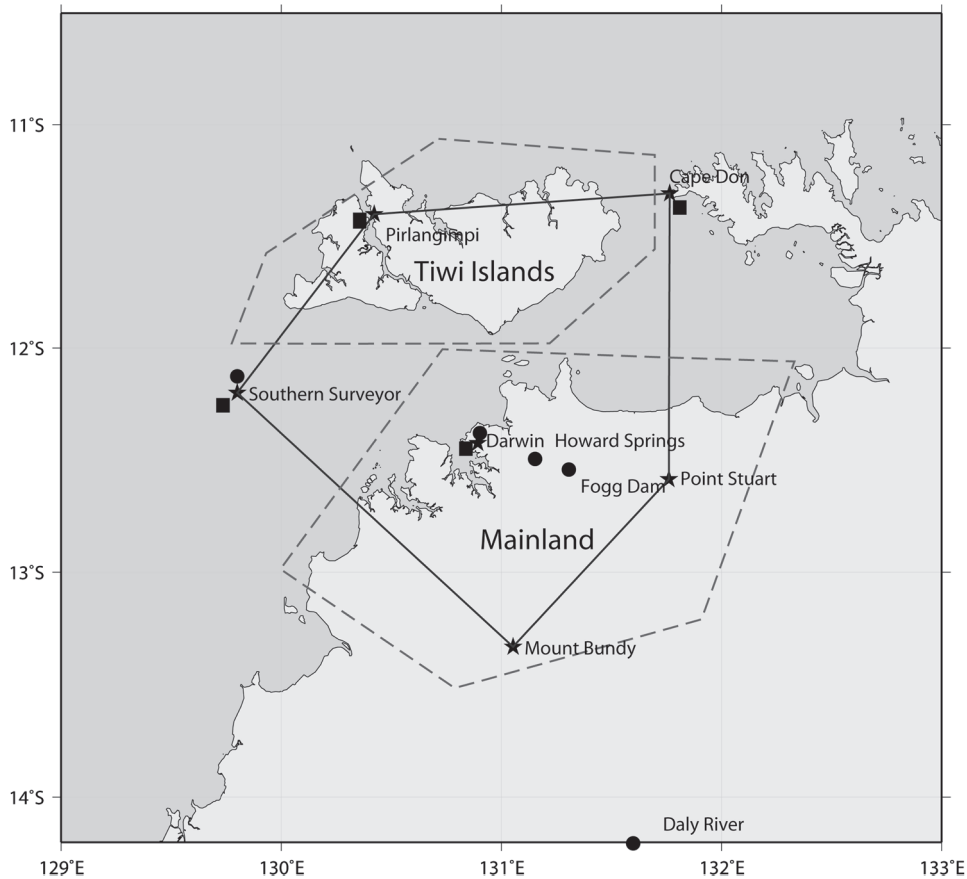
FIG. 1. The ground observation network established during TWP-ICE. The analysis domain is enclosed by the five boundary sounding stations. The mainland subdomain and the Tiwi Islands subdomain are enclosed by the dashed lines. The locations of the sounding, surface radiative flux, and surface turbulence flux stations are displayed as stars, squares, and dots, respectively.

opportunity to study the structure and evolution of these tropical convective systems and their associated environments in an unprecedented level of detail. An overview of TWP-ICE and its synoptic conditions can be found in May et al. (2008).

The focus of this study is to elucidate the variations in the TWP-ICE large-scale structures as well as diabatic heating and drying profiles within the four observed regimes. We attempt to understand how the large-scale atmospheric structure interacts with the organization of the TWP-ICE convective systems and to provide a comprehensive description of the large-scale environment and diabatic heating and drying profiles for future studies on TWP-ICE. An important by-product of the present study are the derived large-scale fields (e.g., vertical velocity and advective tendencies of temperature and moisture), which can be used for heat and moisture budget studies as well as single-column modeling (SCM) and CRM studies of the observed convec-

tive cloud systems. Note that providing such large-scale fields was one of the key goals of the TWP-ICE field campaign (May et al. 2008).

Section 2 provides details about the data and data analysis issues. The synoptic conditions and associated cloud fields are briefly summarized in section 3. Section 4 describes characteristics of the analyzed mean flow and surface conditions. Section 5 examines large-scale structures and diabatic heating and drying profiles exhibited over the four distinct regimes. A further investigation of differences in these fields relative to the diurnal cycle of convection of oceanic, continental/coastal, and island origin is conducted in section 6. Section 7 summarizes the results.

2. Data and data analysis issues

The constrained variational analysis approach of Zhang and Lin (1997) is used to perform an objective analysis of

TWP-ICE data. This method was designed for deriving the large-scale vertical velocity and advective tendencies of temperature and moisture from sounding measurements over a network with a small number of stations. Diabatic heating and drying, or the apparent heat source Q1 and apparent moist sink Q2 as defined by Yanai et al. (1973), can then be estimated as the residuals of heat and moisture budgets of large-scale motion. The variational analysis uses domain-averaged surface and top-of-the-atmosphere (TOA) observations as constraints to adjust atmospheric state variables from soundings by the smallest possible amount to conserve column-integrated mass, moisture, and static energy so that the final analysis dataset is dynamically and thermodynamically consistent. The required observation constraints include the surface and TOA radiative fluxes, surface latent and sensible heat fluxes, and surface precipitation. The variational analysis has been successfully used to process field data collected at the ARM Southern Great Plains (SGP) (Zhang et al. 2001) and North Slope of Alaska (NSA) sites (Xie et al. 2006). It was also used for analyzing data from the TRMM Kwajalein Experiment (KWAJEX), the TRMM Large-Scale Biosphere–Atmosphere Experiment (LBA), and the TRMM South China Sea Monsoon Experiment (SCSMEX) (Schumacher et al. 2007). Details of the variational analysis method can be found in Zhang and Lin (1997) and Zhang et al. (2001). In this section, we provide some technical details about the objective data analysis of TWP-ICE observations to help users better understand the large-scale state dataset developed from this study.

The TWP-ICE sounding array (Fig. 1) provided three hourly soundings during the intensive operational period (IOP) from 22 January to 12 February 2006. The array contains four mainland stations (including the ARM Darwin site), one station on the Tiwi Islands, and one station on the Australian Commonwealth Scientific and Industrial Research Organisation (CSIRO) *Southern Surveyor* ship stationed in the Timor Sea. The sounding array covers an area with a radius of approximately 150 km. The variational analysis technique described above was applied to the sounding IOP over the domain enclosed by the five boundary sounding stations (Fig. 1). In addition, two subanalysis domains were defined to better describe the convective systems of continental/coastal and island origin observed during the break period (respectively the mainland and Tiwi Islands subdomains shown by dashed lines in Fig. 1) since those systems occupied only small regions of the experiment domain as will be shown in the next section. Both continental/coastal and island systems were mainly driven by sea breezes, but the continental coastal systems were also influenced by several squall lines crossing Darwin in

the evening and early morning during TWP-ICE. Therefore, it would be interesting to examine similarities and differences in the structural characteristics of these two types of cloud systems. In the following discussion, the analysis domain refers to the whole TWP-ICE sounding domain unless the mainland or Tiwi Islands subdomains are explicitly indicated. The temporal and vertical resolutions of the analyses used in this study are 3 h and 25 hPa, respectively, for both the sounding domain and the two subdomains.

The variational analysis requires initial analyses of temperature, wind, and humidity for the TWP-ICE domain. These are generated from the TWP-ICE soundings and background European Centre for Medium-Range Weather Forecasts (ECMWF) analyses using an interpolation scheme described by Cressman (1959). The Cressman scheme uses a weighting function that depends on the distance between an observation station and an analysis grid point, as well as the difference between observations and the background. The interpolation is carried out for the difference field between observations and the background. If there is no measurement within a specified distance (L) of an analysis grid point, the scheme will only take the background field as the analysis. The distance L used in this study is 50 km.

The surface and TOA observations, used as the constraints in the variational analysis, were measured by the enhanced surface observation network near Darwin shown in Fig. 1 and the Japanese Multifunctional Transport Satellite (MTSAT), respectively. Among these constraint fields, the surface precipitation rates were derived from a scanning C-band Doppler radar at Gunn Point (near Darwin) using a combination of polarimetric estimators that are dominated by reflectivity at low rain rates, differential reflectivity at moderate rates, and the specific differential phase (KDP) at high rain rates. The particular algorithms are described in Bringi et al. (2001, 2002, 2004). The surface radiation was obtained from radiometer measurements using the algorithm described in Long and Ackerman (2000) and Long (2001). The surface turbulent fluxes were derived from 3D eddy covariance system measurements according to the method described in Beringer et al. (2007). The TOA radiative fluxes were from hourly MTSAT products, which were retrieved using the algorithm described in Minnis et al. (2001).

Since both the C-band polarimetric (C-POL) precipitation radar and MTSAT covered the analysis region completely, a simple arithmetic averaging was used to calculate the domain average precipitation rates and TOA radiative fluxes. For the surface radiative and turbulent fluxes, a weighted average was applied to the data collected from the limited number of surface flux

sites. The weights used in computing the area mean of the surface radiative fluxes were based on the land and ocean fraction within the analysis domain, 0.57 and 0.43, respectively. For the sensible and latent heat fluxes, the weights for data collected at each site (i.e., Darwin Harbour, Fogg Dam, Howard Springs, Daly River, and the ship) were guided by the frequencies of the Moderate Resolution Imaging Spectroradiometer (MODIS) satellite-derived land types within the analysis domain. As shown in Fig. 1, the Daly River site is located outside the analysis domain. However, data collected from the site are important for us to obtain meaningful area-averaged heat fluxes since the Daly River site is surrounded with eucalypt woodland/grassland savanna, one of the most common land types in the Darwin region. The locations of the other four heat flux sites were selected to represent inshore waters (Darwin Harbour), typical northern floodplain (Fogg Dam), eucalypt open forest savanna (Howard Springs), and open ocean (the ship). There were quite large gaps in the surface heat flux measurements. The major missing data periods are 22–25 January 2006 and 1–6 February 2006 at Fogg Dam, 22–23 January 2006 and 1–10 February 2006 at Howard Springs, 22–31 January 2006 at Daly River, 3–7 February 2006 at Darwin Harbour, and 22–25 January 2006 at the ship. The data gaps were filled with ECMWF data, which were adjusted using linear regression equations that were derived for the times when both ECMWF and observations were available.

The Vaisala RS92 sondes used in TWP-ICE are known to have a significant daytime solar radiation dry bias and a minor temperature-dependent calibration error (Vömel et al. 2007). The dry bias is caused by solar heating of the radiosonde's humidity sensor; at the height of 15 km this bias can be as great as 50%. In this study, the dry bias and the temperature-dependent calibration errors in the original RS92 sondes were corrected using an algorithm similar to the one described in Vömel et al. (2007). A radiation dry bias correction factor, a temperature-dependent calibration correction factor, and a solar zenith angle correction factor were applied to the original RS92 sondes (Hume 2007). The largest correction is in the upper troposphere during daylight; however, small changes can also be seen at night and in the lower troposphere mainly because of the use of the temperature-dependent calibration correction factor. More details about the correction can be found in the appendix.

The subdomain large-scale state was derived using the same approach as that used for the entire sounding domain, except that the surface and TOA constraints are averaged over the corresponding subdomains. Sounding data from those stations that are within the specified distance (50 km) of the analysis grid points were used in the analysis through the Cressman method as described earlier. As indicated in Fig. 1, the mean flow and large-scale structures over the mainland subdomain were determined mainly by the sounding data collected at Darwin, Mount Bundy, and Point Stuart, while over the Tiwi Islands subdomain they were determined mainly by the sounding data collected at Pirlangimpi, *Southern Surveyor*, and Cape Don. It is worth noting that the use of subdomain-averaged constraints helps alleviate some of the problems caused by scale aliasing in the measurements over the two smaller subdomains that are originally introduced by the reduction of the number of sounding stations used in the analysis.

It is believed that there are quite large uncertainties in the area-mean surface fluxes because of the limited number of surface flux stations and large data gaps. The small number of surface flux stations cannot well resolve the large spatial variability exhibited in the radiative and heat fluxes in the Darwin region, which contains both ocean and diverse land surface types. Several sensitivity tests were performed to examine the impact of potential uncertainties in the domain-averaged surface fluxes on the derived large-scale structures. In these tests, the area-averaged surface radiative and turbulent fluxes were derived using different weighting coefficients for the data collected from the flux stations. It was found that the derived large-scale fields from these sensitivity tests exhibited very similar temporal and vertical structures with some variations in their magnitudes. The differences between these sensitivity tests and the standard run (which is used in this study) are at least one order of magnitude smaller than typical values of the large-scale fields in the standard run (not shown). This suggests that the analyzed data are suitable for studying large-scale structures for the convection systems observed during TWP-ICE.

3. Synoptic conditions and observed clouds

As described in May et al. (2008), the Darwin region was influenced by a typical monsoonal circulation during TWP-ICE. It experienced four distinct regimes: active monsoon during 13–25 January, suppressed monsoon during 26 January–2 February, clear skies during 3–5 February, and a monsoon break period during 6–13 February. The active monsoon period was characterized by westerly monsoon flow, intensive mesoscale convective systems of mostly oceanic origin, and heavy surface rainfall. During the suppressed monsoon period, an intense low pressure system moved inland to the southwest of Darwin where it deepened, leading to strong westerlies over Darwin as is typical in the days following the

active phase of an MJO. This period was characterized by clouds associated with relatively shallow convection (cloud tops at or below 8 km) accompanied by much lower area-mean precipitation than in the preceding monsoon period. Cirrus resulting from the inland low to the south of Darwin was advected into the TWP-ICE domain. Following the dissipation of the inland low on 3 February, the Darwin region experienced three days of clear skies with no precipitation. This was followed by a monsoon break period, during which an inland heat trough dominated the large-scale conditions over north Australia. Convection during the break period was characterized by intense afternoon thunderstorms with several squall lines crossing Darwin in the evening and early morning.

The cloud and precipitation systems that occurred during TWP-ICE were well observed by the ARM surface remote sensing instruments, including a 35-GHz millimeter wave cloud radar (MMCR), micropulse lidar (MPL), laser ceilometers, and the BOM C-POL radar. Figure 2a shows the time–pressure cross section of observed frequency of occurrence of clouds at the ARM Darwin site. The figure is constructed by integrating measurements from MMCR, MPL, and laser ceilometers using the Active Remotely Sensed Clouds Locations (ARSCL) algorithm (Clothiaux et al. 2000) for the sounding IOP. The integrated products combine the capability of the MMCR to penetrate optically thick hydrometeor layers and the ability of the MPL to detect optically thin clouds (e.g., cirrus). Cloud base shown in Fig. 2a is determined by the MPL and the laser ceilometers, which are usually insensitive to precipitation particles (if they are not sufficiently large) or clutter. As indicated in Clothiaux et al. (2000), the laser ceilometers and MPL can provide quite accurate cloud-base measurements. The area-average surface precipitation rates retrieved from the C-POL radar are shown in Fig. 2b.

Examples of the horizontal distribution of the observed cloud systems and surface rainfall are displayed in Figs. 3 and 4, respectively. The pentagon in these snapshot figures denotes the TWP-ICE sounding domain. It is seen that the major cloud systems and surface rainfall associated with the active monsoon covered much of the analysis region, while those associated with intense afternoon convection and squall lines during the break period only occupied scattered regions (over the mainland and the Tiwi Islands) of the analysis domain. This suggests that the current sounding network might be too big to appropriately describe the break period systems. This motivated the analysis over the mainland subdomain and the Tiwi Islands subdomain carried out in section 6.
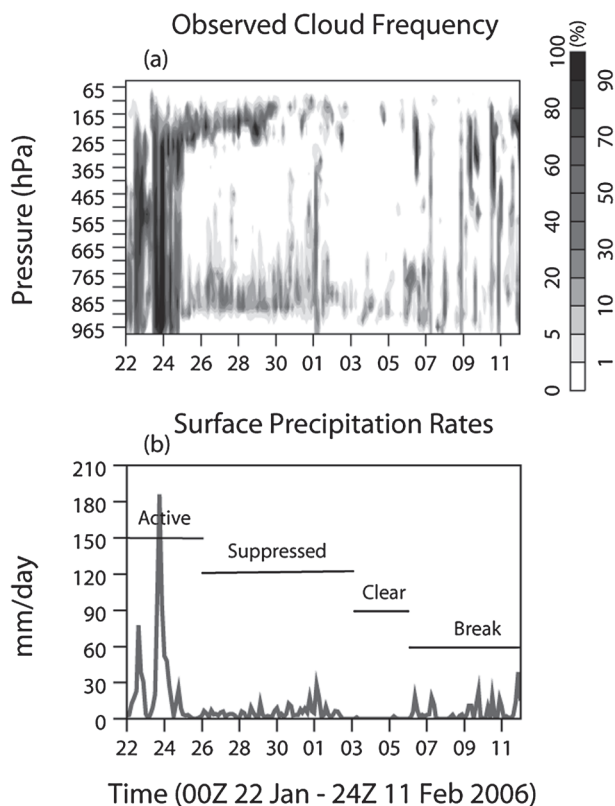

FIG. 2. (a) Observed cloud frequency at Darwin from the ARM surface remote sensing instruments (MMCR, MPL, and laser ceilometer) and (b) the domain-averaged surface precipitation rates from the BOM C-POL radar. The four regimes are marked in (b).

4. Mean flow and surface conditions

The large-scale environment of the Australian summer monsoon as analyzed with the variational analysis is shown in Figs. 5a–c, which display the analyzed zonal and meridional wind components and relative humidity (RH) fields, respectively. RH is calculated with respect to ice for $T < 0°C$. Note that the analyzed data represent an average over the analysis domain as shown in Fig. 1. A 24-h running smoothing was applied to all fields for display purposes.

The analyzed winds clearly demonstrate the northern Australia summer monsoonal flow observed during TWP-ICE. The monsoon period (active, suppressed, and clear skies) was characterized by westerlies at low- to midlevels, whereas the break period was characterized by easterlies at the levels above 915 hPa. The easterly flow observed on 24 January at the levels above 915 hPa was due to the monsoon trough retreating to the north of Darwin (May et al. 2008). A strong westerly wind event was observed during the suppressed monsoon period, following the active phase of an MJO. At the same time, an easterly flow occurred in the upper
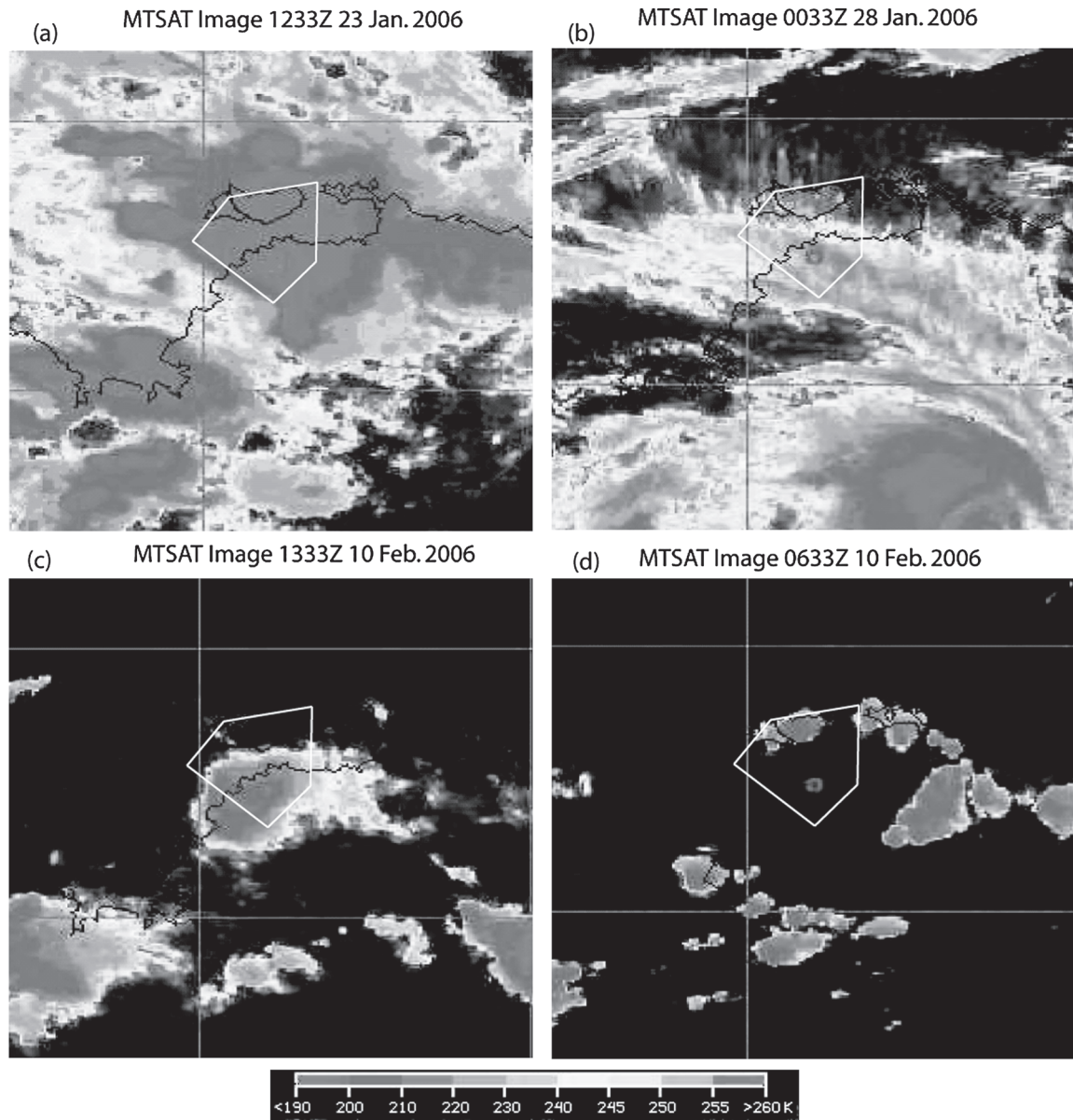
FIG. 3. Four snapshots showing the satellite images for the different cloud systems observed during (a) the active; (b) suppressed; and (c),(d) break periods. The pentagon in these figures denotes the TWP-ICE sounding domain. Local time in Darwin is 9.5 h greater than universal time. Black represents clear-sky area.

troposphere. The meridional wind component is much weaker than the zonal wind component, typically less than 5 m s^{-1} in the troposphere (Fig. 5b). The temporal and vertical structure of RH shows a strong association with the observed cloud fields (Fig. 2). The RH was usually larger than 80% throughout the troposphere during the active monsoon period. Low RH values were seen in the midtroposphere during the suppressed, clear skies, and break periods. The dry air was likely related to dry intrusions originated from higher latitudes, which are often observed over the tropical western Pacific

(Numaguti et al. 1995). The dry midtroposphere could act to suppress the convection and prevent the formation of deep cumulus clouds.

Figures 6a–d show the analyzed domain-averaged surface temperature, surface wind speed, sensible heat flux, and latent heat flux, respectively. These surface fields exhibited notable differences over the four regimes. For example, the break period had higher surface temperature and sensible heat flux but weaker surface wind and latent heat flux compared to the active and suppressed monsoon periods. It is seen that the
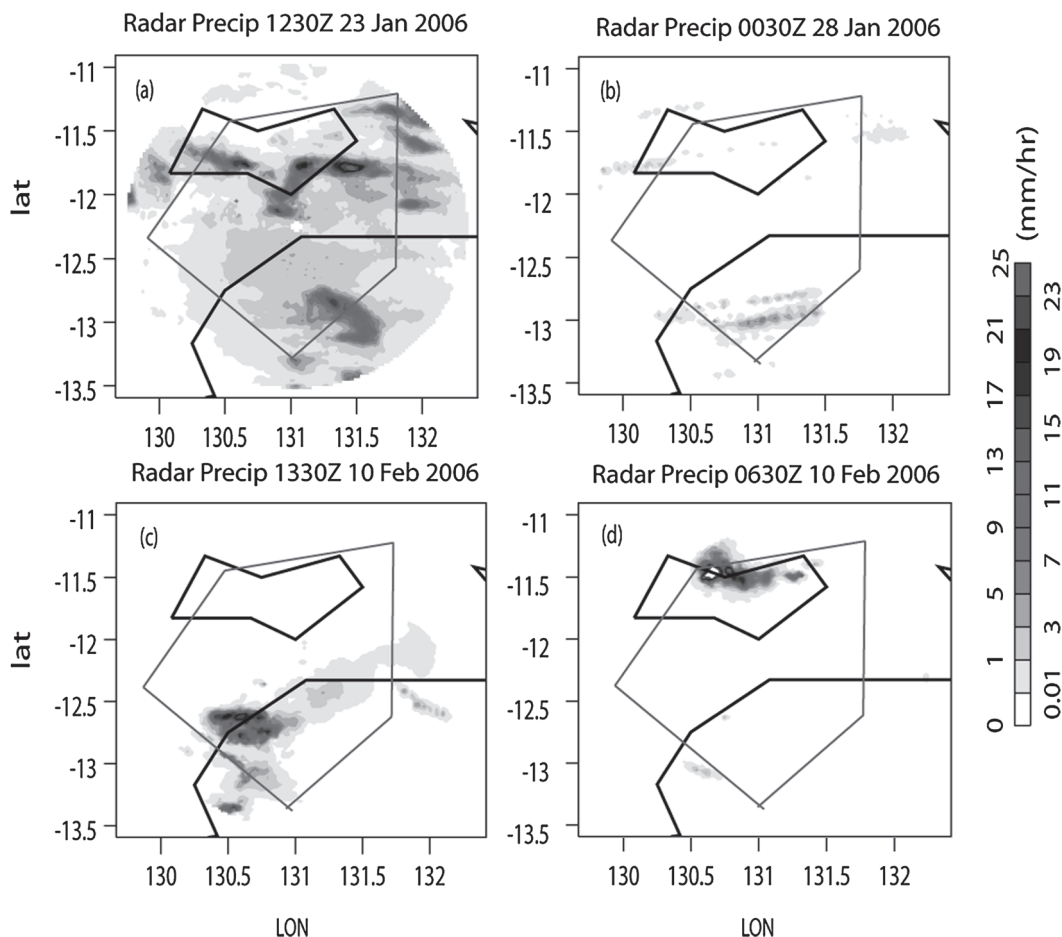
FIG. 4. Images of the C-POL radar precipitation for the similar times as the satellite pictures shown in Fig. 3. The pentagon in these figures denotes the TWP-ICE sounding domain. Local time in Darwin is 9.5 h greater than universal time.

sensible heat flux showed some correlation with the surface temperature, whereas the surface latent heat flux was better correlated with the surface wind speed. Both the surface wind and latent heat flux (or evaporation) were significantly enhanced following the passage of the active phase of the MJO event. The increase of surface temperature with time was consistent with an increase of net surface shortwave radiation (Fig. 7a) due to a decrease of cloud fraction especially at low levels. The reduction of clouds from the active monsoon to the break period also led to an increase of net downward shortwave and outgoing longwave radiative fluxes at TOA (Figs. 7b and 7d, respectively) and an increase of net surface upward longwave radiation (Fig. 7c).

Associated with the activity of a major MJO event over the Darwin region, the observed characteristics of the large-scale environment during the active and suppressed monsoon period of TWP-ICE show many similarities to those observed over the tropical western Pacific warm pool region, such as those described in Lin and Johnson (1996a) for the Tropical Ocean and Global Atmosphere Coupled Ocean–Atmosphere Response Experiment (TOGA COARE) conducted over the western Pacific warm pool, in which the large-scale circulation was also largely impacted by major MJO events. For example, both TWP-ICE and TOGA COARE data show significantly increased westerlies and evaporation following the active phase of an MJO event. This indicates that the TWP-ICE data could help understand tropical convective systems that occur over the warm pool region. However, they differ significantly during the break period, where TWP-ICE had the unique continental/coastal and island-initiated convective systems that occurred in the Darwin region almost on a daily basis. Data collected from TWP-ICE provide a unique opportunity to study these tropical land systems and their associated environments.
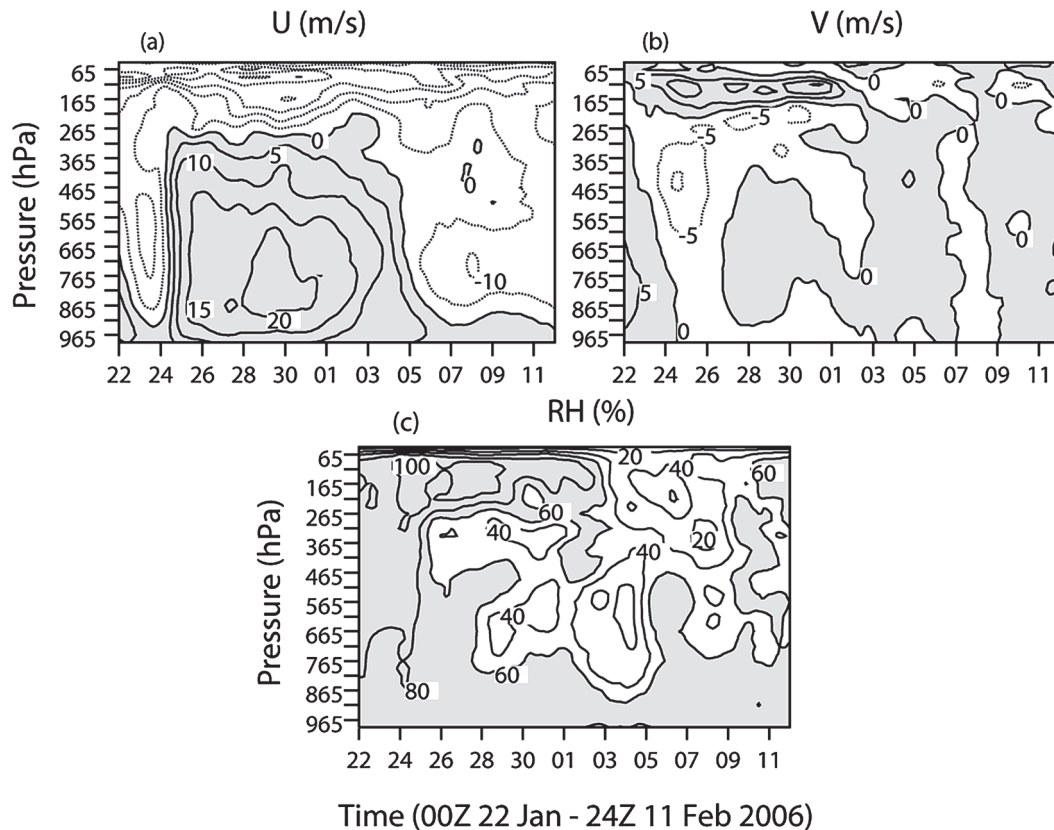
FIG. 5. The time–pressure cross sections of the analyzed large-scale state fields over the sounding domain during TWP-ICE. (a) Zonal wind, (b) meridional wind, and (c) relative humidity (with respect to ice for $T < 0°C$). In these figures, solid lines are for values larger than or equal to zero and dotted lines for values less than zero. In (a) and (b), positive values are shaded and in (c) values larger than 60% are shaded. Contour interval is 5 in (a) and (b) and 20 in (c). A 24-h running mean was applied to these fields.

5. Mean large-scale structures and diabatic heating and drying profiles

One of the major goals of TWP-ICE is to determine mean large-scale dynamic and thermodynamic structures and diabatic heating and drying profiles associated with tropical convective cloud systems. Details of the vertical heating profile are known to have large influence on both tropical weather and climate systems and are central to their intraseasonal variability (Yanai et al. 2000; Lin et al. 2004). In this section, we examine the evolution of the derived large-scale state and diabatic heating and drying as well as their vertical structures over the four distinct regimes.

The temporal evolution and period-averaged large-scale vertical velocity derived from TWP-ICE observations over the whole sounding domain are shown in Figs. 8a and 8b, respectively. The mean vertical velocity field during the active monsoon period showed strong upward motion through the entire troposphere with maximum around 265 hPa (Fig. 8b). In contrast, the av-

erage vertical motion was weak during the suppressed, clear, and break periods. The suppressed monsoon period was characterized by moderate upward motion below 665 hPa and above 245 hPa and weak downward motion in the midtroposphere. Compared to the suppressed period, the three clear days had stronger downward motion above 465 hPa and weaker upward motion below 665 hPa. During the break period, moderate midlevel upward motion occurred with virtually no vertical velocity below 765 hPa in its averaged profile. The characteristics of the vertical velocity field during the monsoonal period are similar to those shown in TOGA COARE (Lin and Johnson 1996a) in which the upward motion maxima were found at upper levels during the active convective period, and low-level weak upward motion or subsidence was observed during suppressed convective period when strong westerly winds prevailed. The major difference between these two datasets is that the ascending maximum of the TWP-ICE profile occurs higher (265 hPa), indicating higher clouds or stronger updrafts, than that of the TOGA

Surface Temperature
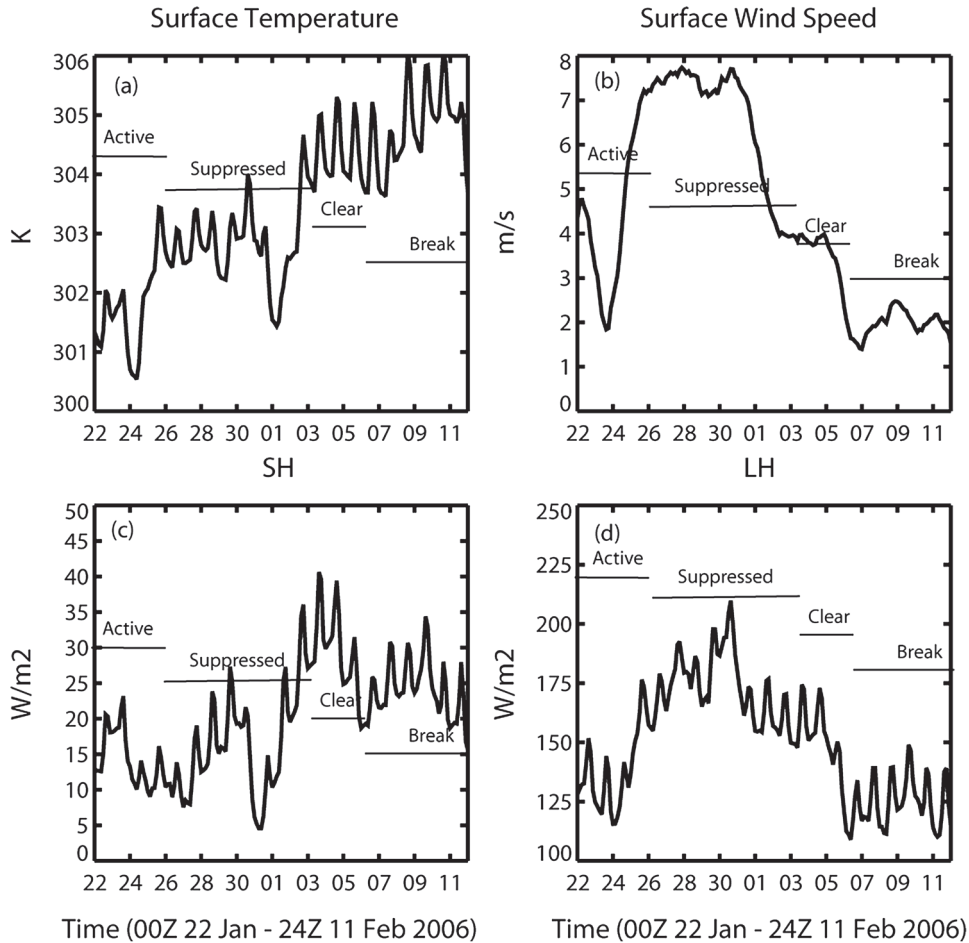

Surface Wind Speed

SH

LH

FIG. 6. Time series of (a) analyzed surface temperature, (b) surface wind speed, (c) surface sensible heat flux, and (d) surface latent heat flux, over the sounding domain during TWP-ICE. A 24-h running smoothing was applied to these fields.

COARE profile (350 hPa) during the active convection period.

Figure 9 displays the analyzed total advective temperature tendency (T_{adv_tot}) and its horizontal component (T_{adv_hori}), which are defined as

$$T_{adv\_tot} = -\mathbf{V}_h \cdot \nabla_p T - \omega \frac{\partial T}{\partial p} + \frac{\omega}{\rho Cp}$$

$$= T_{adv\_hori} - \omega \frac{\partial T}{\partial p} + \Delta T_{adiab}, \qquad (1)$$

where T is the temperature, $\mathbf{V}_h$ is the horizontal wind vector, ΔT_{adiab} is the adiabatic compression term, p is the pressure, and ω is the vertical velocity in p coordinates. The total advective temperature tendency was mainly dominated by its vertical component (including the adiabatic compress term) during the active and break periods as the horizontal advective tendency of temperature was relatively weak. For the active mon-

soon period, the entire column was cooled primarily by vertical advection with the maximum cooling between 340 and 565 hPa (Fig. 9c), whereas for the break period moderate cooling was seen only at midlevels. Unlike the active and break periods, the suppressed period experienced pronounced horizontal advective cooling between the surface and 215 hPa (Fig. 9d). The total advective cooling rate decreased with height above 765 hPa, with the largest cooling occurring in the lower troposphere (Fig. 9c). Another interesting feature seen in Fig. 9d was that the boundary layer was largely cooled by horizontal advection during the three clear days.

Figure 10 shows the temporal evolution and period-averaged total and horizontal advective tendencies of moisture, q_{adv_tot} and q_{adv_hori}, which are defined as

$$q_{adv\_tot} = -\mathbf{V}_h \cdot \nabla_h q - \omega \frac{\partial q}{\partial p} = q_{adv\_hori} - \omega \frac{\partial q}{\partial p}, \qquad (2)$$
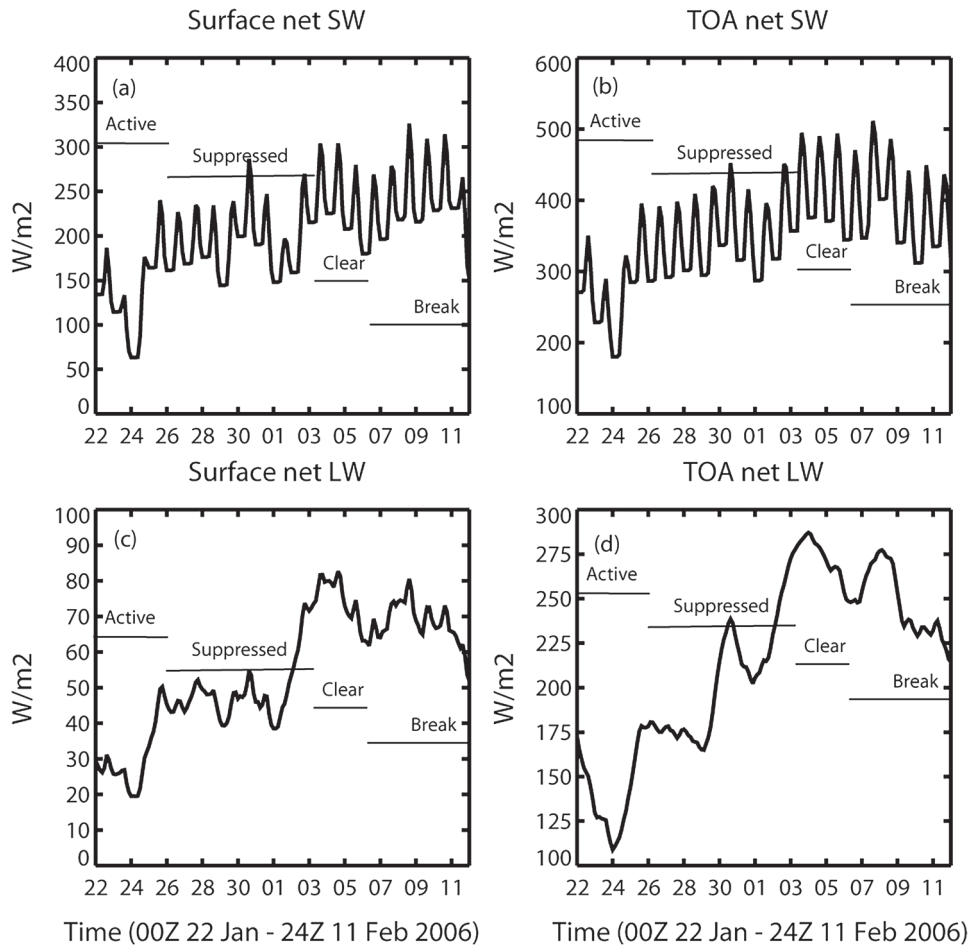
FIG. 7. Time series of (a) analyzed surface net shortwave radiative flux, (b) TOA net shortwave radiative flux, (c) surface net longwave radiative flux, and (d) TOA net longwave radiative flux, over the sounding domain during TWP-ICE. A 24-h running smoothing was applied to these fields.

where q is water vapor mixing ratio. For the active period, strong moistening existed through the entire troposphere with two peaks respectively at around 715 and 465 hPa. For the break period, the moistening was mainly located at midlevels and was associated with weak drying in the boundary layer. Notable midlevel drying with the peak around 615 hPa was found for the suppressed period and significant low-level drying was found over the three clear days (Fig. 10c). The drying tendencies were primarily due to the large horizontal advection seen during these two periods (Fig. 10d). The mid- and low-level horizontal dry advection would seem to be partially responsible for the substantially dry midtroposphere seen in the RH field during the suppressed monsoon period. It is interesting to see from Fig. 10d that basically all the four subperiods experienced horizontal dry advection, indicating that the moistening tendencies shown in Fig. 10c were from vertical advective tendencies of moisture.

The diabatic heating (Q1) and drying (Q2) derived from the variational analysis are given in Figs. 11 and 12, respectively. The Q1 and Q2 fields showed significant variations over the four different regimes. The heating and drying were strongest during the active monsoon period, consistent with the heaviest rain produced there. The averaged Q1 profile of the monsoon systems exhibited a maximum between 340 and 540 hPa. The upper-level heating peak was associated with both deep convection and stratiform precipitation. The shape of the mean profile of the active monsoon cloud systems is very similar to that diagnosed from other tropical regions, for example, the heating profiles derived from the AMEX systems (Frank and McBride 1989) and the TOGA COARE systems (Lin and Johnson 1996b), which all had maximum heating in the mid- and upper troposphere.

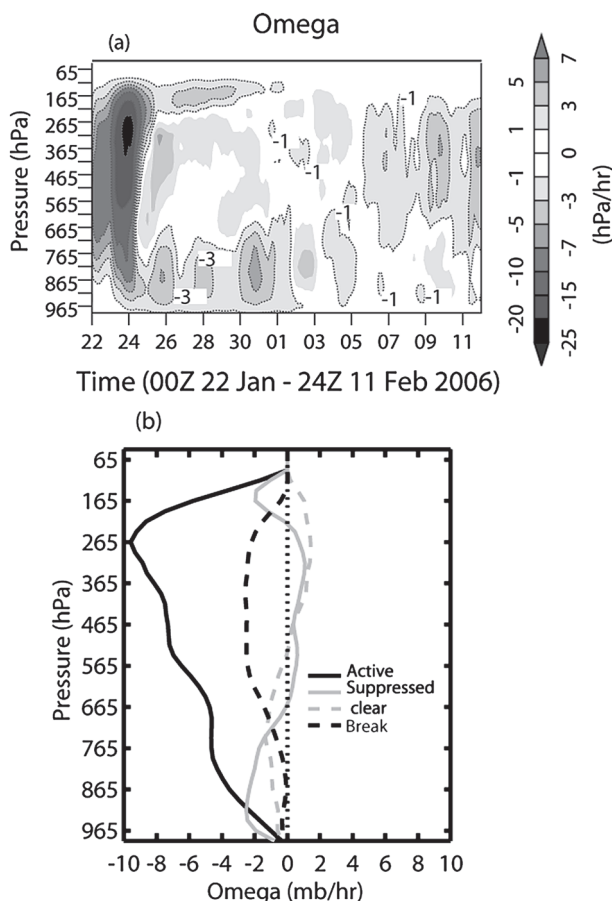The Q2 profile of the monsoon systems showed two major drying layers: one above 565 hPa and another one

Omega

FIG. 8. Analyzed vertical velocity over the sounding domain during TWP-ICE. (a) Temporal evolution (dotted lines for values less than -1 hPa hr^{-1}); (b) averaged profiles for different periods.

below 665 hPa. The relative minimum in Q2 between 565 and 665 hPa corresponds to the minimum in the total moisture advection. The double-peak structure in Q2 is similar to that observed in tropical convective systems over the Marshall Islands (Yanai et al. 1973) and northern Australia during AMEX (Frank and McBride 1989). As suggested in Johnson (1984), the double-peak structure might be related to cumulus updrafts that contribute to the lower peak and mesoscale updrafts that result in the higher one. It is noted that the drying maximum occurred at levels just slightly lower than the heating maximum, implying a significant contribution from stratiform rain to the Q2 profile.

Compared to the active monsoon period, the heating was moderate and was confined above 700 hPa for the break period. Below this level, weak cooling was observed. The cooling was likely related to evaporation of shallow cumulus clouds and convective and mesoscale downdrafts, which also led to moderate moistening there. The heating and drying during the suppressed period was

mainly located at low levels, consistent with the prevalence of shallow cumulus clouds. Quite strong moistening was observed at midlevels, likely associated with evaporation from the low- and midlevel clouds. For the clear days, moderate cooling was seen above 565 hPa, presumably because of clear-sky radiative cooling, and strong moistening was found around 815 hPa. Note that the "clear days" had nonprecipitating shallow convection, as indicated by ARSCL (Fig. 2a). The strong similarity between Q2 and q_{adv_hori} suggests that convection is countering the effects of horizontal dry air advection.

6. The diurnal cycle of oceanic, mainland, and island-initiated cloud systems

The 3-hourly radiosonde launches during TWP-ICE provide a unique opportunity to study the diurnal cycle of the cloud systems observed during the northern Australian monsoon season. In this section, we focus our analysis on the diurnal cycle of the large-scale structures and diabatic heating and drying profiles with those convective cloud systems that occurred under different surface boundary conditions. The convective systems examined include the intensive monsoon systems of oceanic origin that occurred between 0000 local standard time (LST) 22 January and 2400 LST 25 January during the active monsoon period and the mainland and island-initiated convective systems that were observed between 0000 LST 6 February and 2400 LST 11 February during the break period. To more appropriately describe the mainland and island-initiated convection we carried out additional analyses for the two smaller subregions shown in Fig. 1. The results of these analyses will be used here and will be referred to as the mainland domain and the Tiwi Islands domain, respectively. For the large-scale monsoon cloud systems, the analysis data over the whole sounding domain are used. In the following discussions, we use the term "mainland systems" to refer to those convective systems that occurred over the mainland domain and "island systems" to refer to those convective systems that were observed over the Tiwi Islands domain during the break period.

a. Precipitation

According to earlier studies (e.g., Nesbitt and Zipser 2003), tropical precipitation tends to peak in the afternoon over land areas because of afternoon boundary layer destabilization caused by daytime insolation and in the early morning over adjacent ocean regions associated with the long, nocturnal life cycle of mesoscale convective systems. Similar diurnal features are seen in the convective systems observed during TWP-ICE
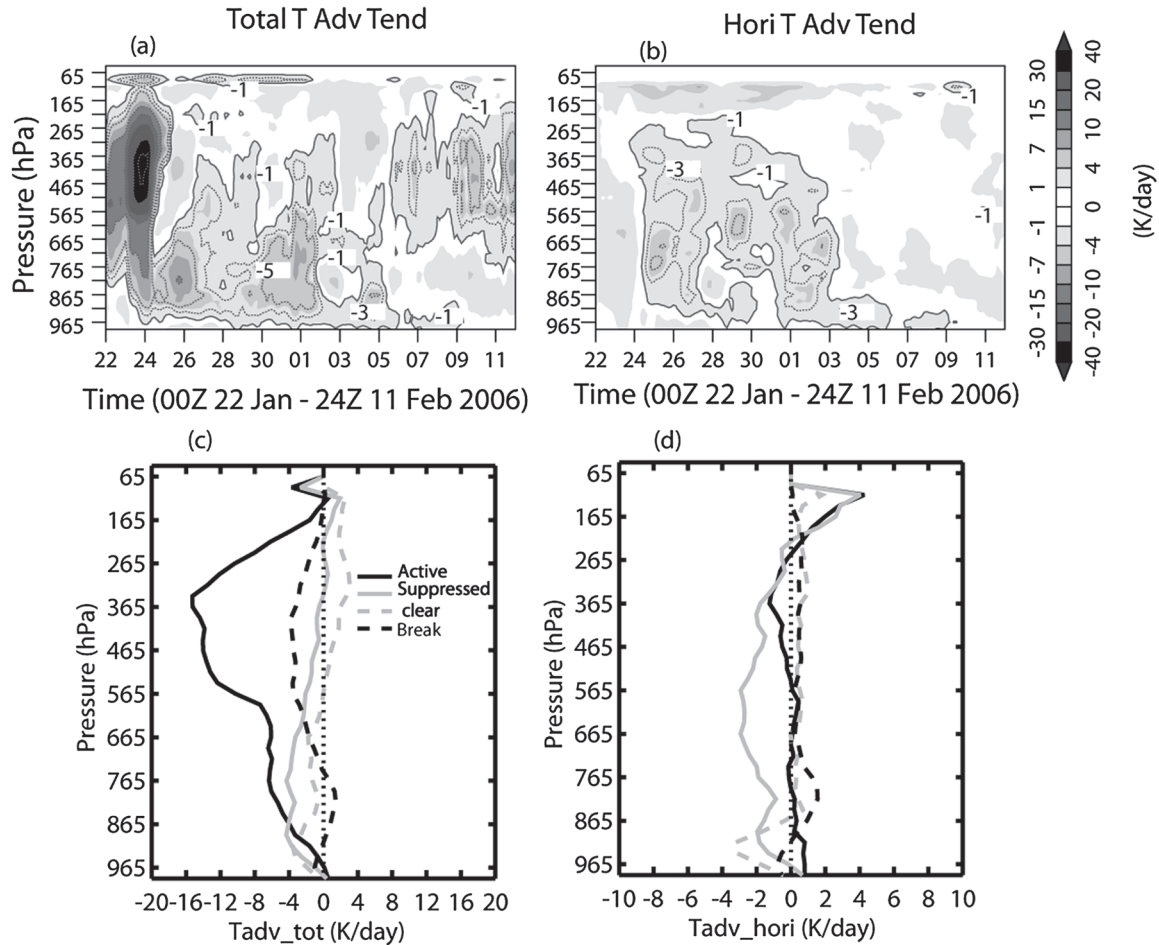
FIG. 9. Analyzed advective tendency of temperature over the sounding domain during TWP-ICE. (a) Temporal evolution of total advective tendency of temperature; (b) temporal evolution of horizontal advective tendency of temperature. In (a) and (b), dotted lines for values less than -1 k day^{-1}. (c) Averaged total tendency profiles for different periods; (d) averaged horizontal tendency profiles for different periods.

(Fig. 13). The monsoon precipitation associated with intensive mesoscale convective systems tends to peak in the early morning hours (around 0300 LST), while the island precipitation reaches its maximum value at 1500 LST in the afternoon. In contrast, the mainland precipitation shows a semidiurnal variation, with one peak in the early morning (0600 LST) and the other one in the late afternoon (1800 LST). The daytime convective systems over the mainland and Tiwi Islands domains were mainly driven by sea breezes due to the differential heating between the ocean and the land. Shallow cloud systems tended to form around midmorning (around 0900–1000 LST) along the coast and then developed into precipitating deep convective systems in the afternoon. The time for coastal convective clouds to propagate into inland likely results in the 3-h delay for the mainland precipitation to reach its maximum compared to the island systems. The early morning peak seen in the main-

land precipitation is associated with the passage of squall lines that originated outside the measurement domain (May et al. 2008).

b. Cloud frequency

The diurnal cycle in the profiles of cloud occurrence (Figs. 14a,b) is computed from the ARM cloud measurements at the Darwin site. The single-point measurements can be considered to roughly represent the monsoon clouds (which usually covered a large fraction of the experimental domain) and the clouds associated with the coastal systems over the mainland because of their proximity to the measurement site. There were no cloud observations over the Tiwi Islands domain.

Significant diurnal variations are seen in cloud occurrence for both the monsoon and mainland systems. The monsoon system has significant amounts of clouds through the troposphere at night and relatively few clouds
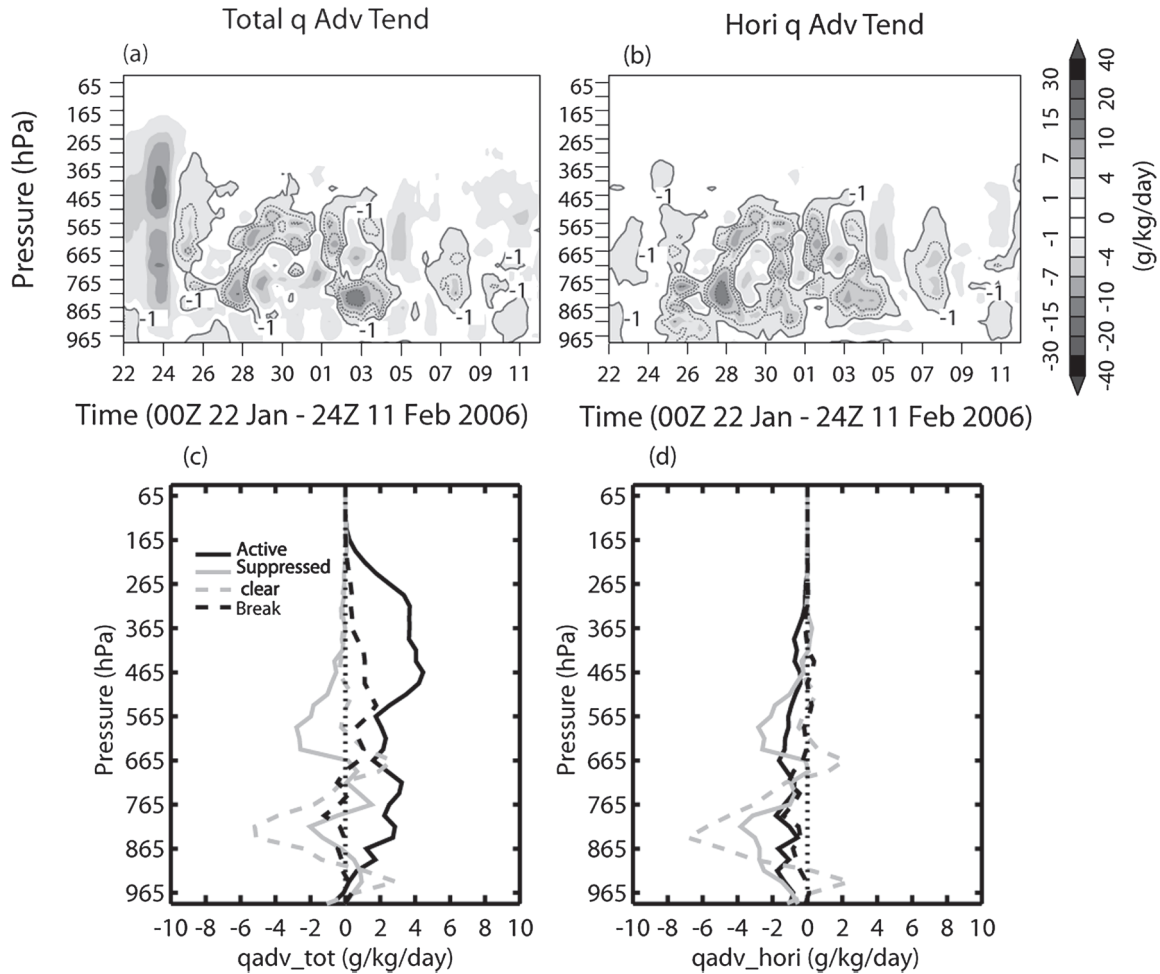
Total q Adv Tend

(a)

Hori q Adv Tend

(b)

FIG. 10. Same as Fig. 9 except for the advective tendency of moisture.

during the day, consistent with the diurnal variation of the monsoon precipitation as shown in Fig. 13. In contrast, the diurnal evolution of the mainland clouds displays a clear progression from shallow to deep convection during the day: shallow cumulus clouds grow atop the daytime boundary layer and then develop into deep convective clouds in the late afternoon. It is interesting to see that the mainland clouds peak at midnight with the prominent maximum value seen in upper troposphere rather than peak around the time of the maximum precipitation. This might reflect the fact that the sea-breeze precipitation has moved inland away from Darwin so that the ARM Darwin site only observes the high clouds that have advected over the site from the deep convection that is further inland. The clouds seen at night and in the early morning hours are also related to the passage of squall lines over the mainland domain. It is noted that there is a general lack of midlevel clouds in the mainland systems. This might be due to the dry

midtroposphere observed during the break period, as shown in Fig. 5c.

c. Vertical velocity

Consistent with the convective activity, Figs. 15a–c show strong diurnal variations in the large-scale vertical velocities associated with the three types of convective systems. For the monsoon systems, the large-scale environment is characterized by upward motion throughout the troposphere over the composite period. Upward motion is weak during the day. It increases rapidly in the evening (around 2100 LST) associated with the development of nocturnal deep convection. The strongest ascent is seen in the upper troposphere between 265 and 465 hPa at 0300 LST when precipitation reaches its maximum intensity. The upward motion then decreases gradually between 0300 and 1200 LST while the maximum ascent still remains above 565 hPa, corresponding to the development of stratiform clouds.
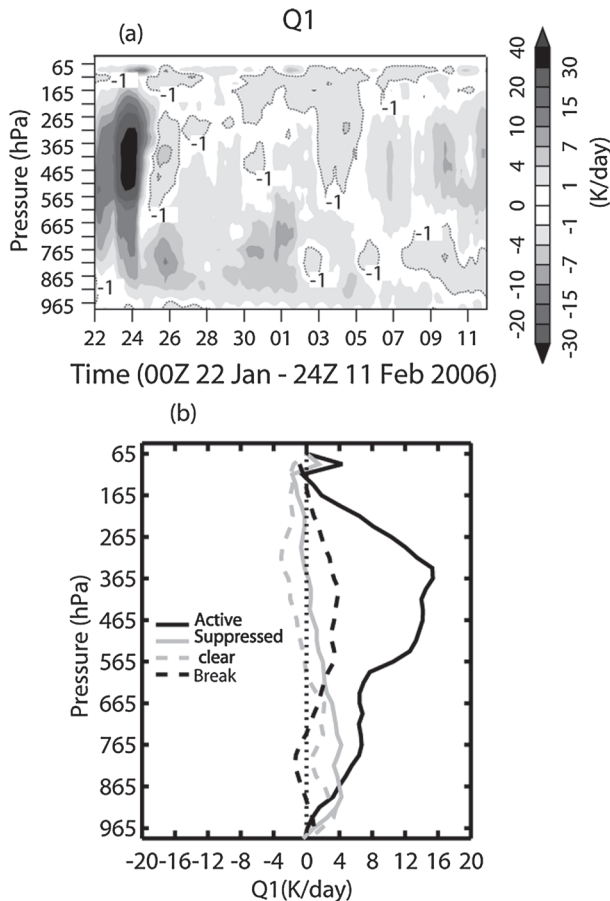
FIG. 11. Analyzed diabatic heating rate (Q1) over the sounding domain during TWP-ICE. (a) Temporal evolution (dotted lines for values less than −1 k day^{-1}). (b) Averaged profiles for different periods.

FIG. 12. Analyzed diabatic drying rate (Q2) over the sounding domain during TWP-ICE. (a) Temporal evolution (dotted lines for values less than −1 k day^{-1}). (b) Averaged profiles for different periods.

The mainland systems exhibit a layer of weak vertical motion at low levels in the midmorning (around 0900 LST) that is presumably related to the low-level convergence caused by the sea breezes. Interestingly there is a subsidence layer at midlevels in the late morning and early afternoon that contributes to confining the mainland convection to low levels and presumably also prevents convection from developing spontaneously anywhere in the domain at the initial stage. As the sea-breeze system develops, quite strong upward motion is observed in the levels above 665 hPa with weak vertical motion below. The upward motion peaks at 1500 and 2400 LST with the afternoon peak (around 315 hPa) higher than the midnight peak (around 465 hPa). It is noted that the peaks in vertical velocity occur a few hours earlier than those in precipitation for the mainland systems, indicating a time lag between the dynamic structure and the formation of significant rainfall over the mainland region.
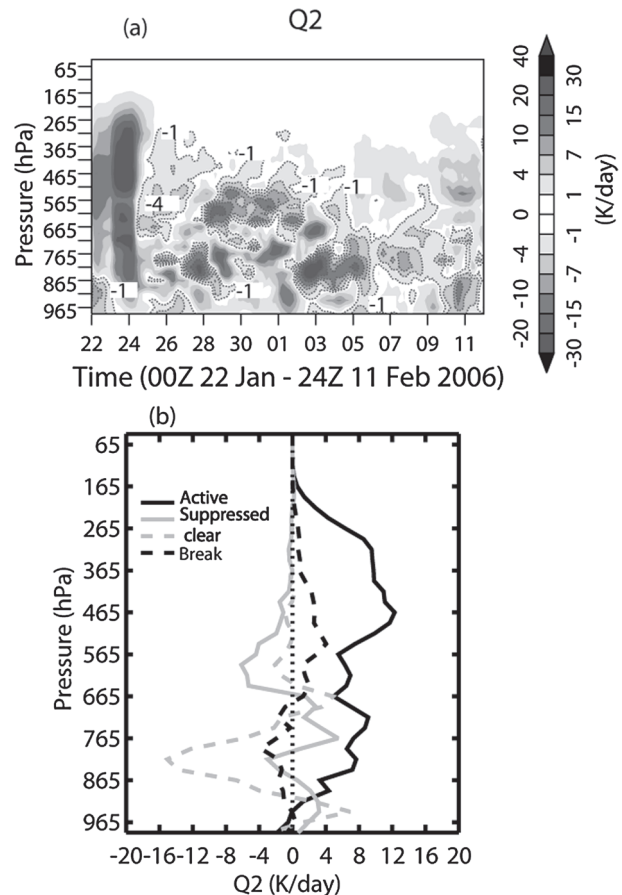
The diurnal cycle of vertical velocity for the island systems is quite different from that of the mainland systems. The island systems display a strong diurnal variability in vertical velocity in the mid- and upper troposphere. The strongest upward motion is seen around 465 hPa at 1500 LST when the surface precipitation reaches its maximum and the downward motion peaks around 415 hPa between 0600 and 0900 LST. The upward motion remains weak and constant below 665 hPa during most of the day except for midnight and the early morning hours. This is different from the mainland systems, which show a moderate subsidence layer below 665 hPa near noon. Compared to the mainland systems, the island systems show a much deeper ascending layer in the lower troposphere during the day and a more significant subsidence layer in the mid- and upper troposphere in the midmorning (0900–1000 LST) when convection starts. The subsidence layer acts to restrict the island convection at low levels (shallow convection) at its initial stage,
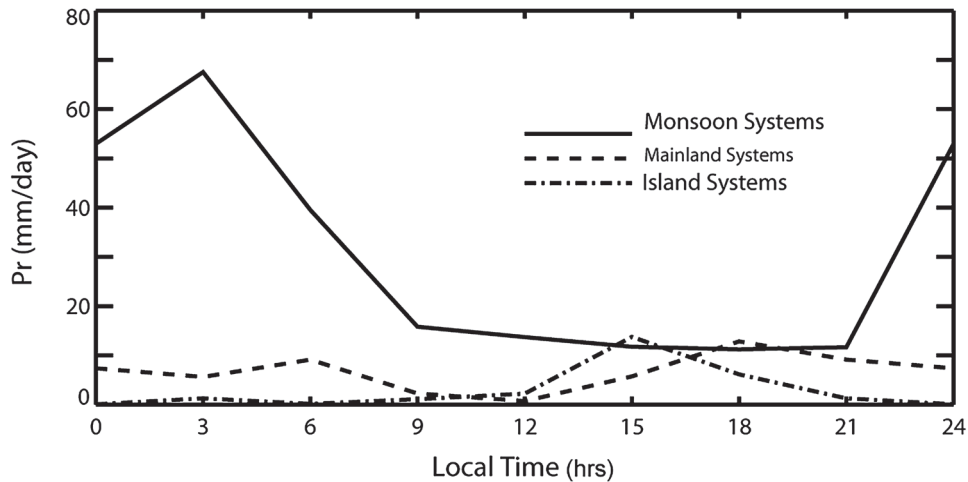
FIG. 13. Diurnal cycle of surface precipitation rates (mm day^{-1}). Solid line is for monsoon systems, dashed line is for mainland systems, and dot–dashed line is for island systems.

similar to the mainland convection. This is consistent with the results from earlier studies (e.g., Simpson et al. 1993), which indicated that the island-initiated convection was characterized by widespread shallow convection at its initial stage over the islands.

d. Advective tendencies of temperature and moisture

The diurnal variation of the total advective tendency of temperature generally resembles that of the vertical velocity field with advective cooling corresponding to upward motion and advective warming corresponding to downward motion (not shown). This is consistent with the fact that the horizontal advection of temperature was very weak during these two periods.

Similarly, the diurnal variation of the total advective tendency of moisture for the monsoon systems (Fig. 16a) also resembles that of the vertical velocity field. Strong advective moistening is seen in the mid- and upper troposphere at night and weak drying is found below 800 hPa during the day. The atmospheric moistening shown in the monsoon systems is primarily due to the vertical advection of moisture because the horizontal terms (Fig. 17a) generally show advective drying in the mid- and upper troposphere, while the daytime lower-level drying is mainly associated with dry horizontal advection of moisture. In contrast, both the mainland and island-initiated systems show a weak moistening layer near the surface and a moderate drying layer above during the day in both the total and horizontal advection fields (Figs. 16b,c and 17b,c). Compared to the mainland systems, the island systems show considerably stronger total and horizontal advective moistening below 865 hPa over the composite period and weaker drying in the low and midtroposphere during the day. It is interesting to note

that there exists a minimum in total advective moistening near 600 hPa for the monsoon system (Fig. 16a). This is caused by the persistent maximum relative humidity observed at that level (not shown). The moistening minimum results in a distinct double-peak structure in the total moisture advection profile for the monsoon systems when they reach the maximum intensity between midnight and 0300 LST.

e. Heating and drying profiles

The composite profiles of the diurnal cycle of diabatic heating for the three periods are shown in Figs. 18a–c, respectively. The Q1 profiles are largely influenced by the vertical velocity. For the monsoon systems (Fig. 18a), the heating is weak during the day and reaches its maximum at 0300 LST when the strongest precipitation occurs. The maximum heating is seen in the upper troposphere between 365 and 465 hPa. In contrast, the upper-level maximum heating occurs in the afternoon around 1500 LST for the mainland systems (Fig. 18b), associated with the development of intensive afternoon deep convection. In the morning (0900–1200 LST), the heating is mainly located near the surface because of the occurrence of shallow convection. The heating and cooling seen at night are related to the passage of squall lines. Compared to the mainland systems, the island systems (Fig. 18c) also exhibit a diabatic heating layer near the surface in the morning associated with the development of shallow convection. The heating rapidly extends to the mid- and upper troposphere as convection develops and reaches its maximum in the afternoon (around 1500 LST). Diabatic cooling dominates the entire troposphere at night for the island systems. This is different from the mainland systems.
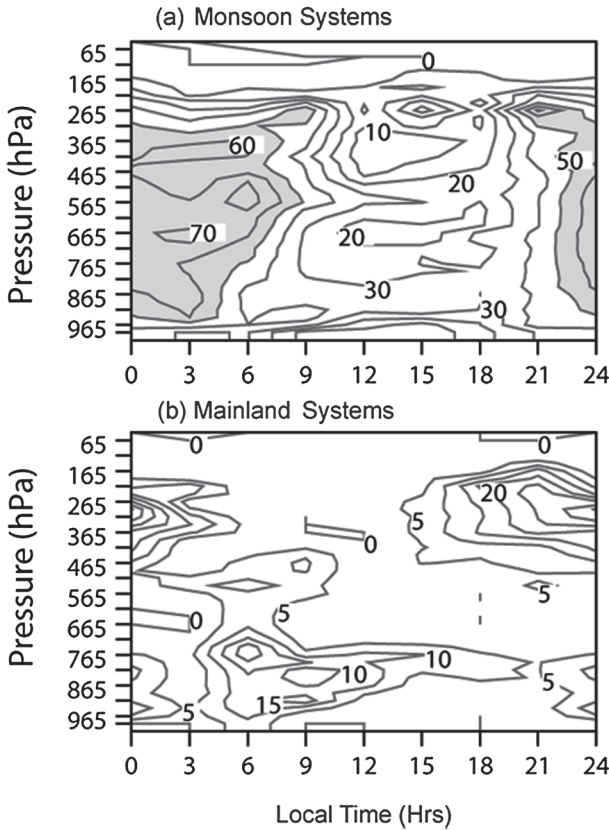
FIG. 14. Diurnal cycle of clouds. (a) Monsoon systems and (b) mainland systems. The unit is %. In the figures, values larger than 50% are shaded. Contour interval is 10 in (a) and 5 in (b).

The composite profiles of diurnal cycle of diabatic drying for the three types of systems are shown in Fig. 19. The variations of the vertical profiles of Q2 resemble those of the total advective tendency of moisture. All the systems show considerable moistening (particularly for the mainland and island systems) in the lower troposphere during the day with the peak seen around local noon. This low-level moistening is presumably due to the evaporation of shallow cumulus clouds or boundary layer processes. In the mid- and upper troposphere, the monsoon systems display a prominent maximum drying at midnight because of nocturnal deep convection, while both the mainland and island systems exhibit a pronounced maximum drying in the afternoon.

7. Summary

We have documented the large-scale structure and diabatic heating and drying profiles of the tropical convective systems observed during TWP-ICE, which was conducted in January and February 2006 in Darwin during the Australian summer monsoon season. Our analysis has focused on the variations of the structures with dif-
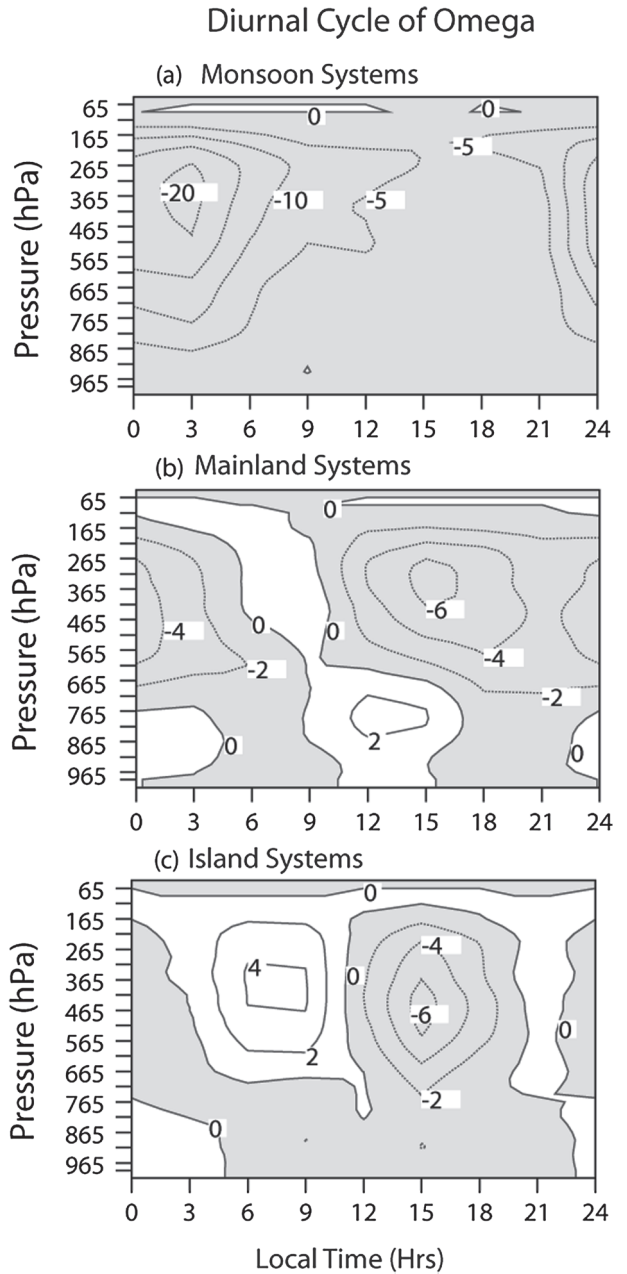

FIG. 15. Diurnal cycle of vertical velocity (hPa hr^{-1}). (a) Monsoon systems, (b) mainland systems, and (c) island systems. In (a)–(c), negative values are shaded. Contour interval is 5 in (a) and 2 in (b) and (c).

ferent synoptic regimes experienced in Darwin during the experiment. The monsoon behavior during the experiment was found to be modulated by the passage of an MJO event. A constrained objective variational analysis approach was used to derive the large-scale state and Q1 and Q2 profiles from original sounding measurements.

It is shown that the Darwin region had a very similar environment to that observed in other tropical regions
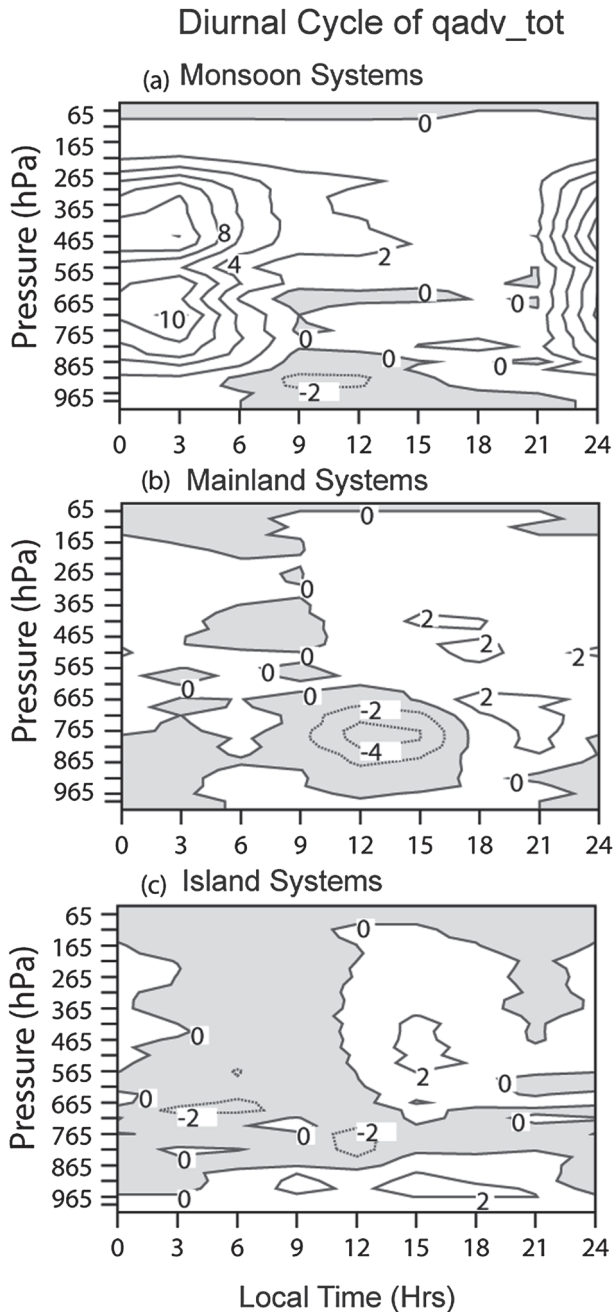
Diurnal Cycle of qadv_tot

FIG. 16. Diurnal cycle of total advective tendency of moisture (g kg^{-1} day^{-1}). (a) Monsoon systems, (b) mainland systems, and (c) island systems. In (a)–(c), negative values are shaded. Contour interval is 2 in these figures.

Diurnal Cycle of qadv_hori

FIG. 17. Diurnal cycle of horizontal advective tendency of moisture (g kg^{-1} day^{-1}). (a) Monsoon systems, (b) mainland systems, and (c) island systems. In (a)–(c), negative values are shaded. Contour interval is 1 in these figures.

during the active and suppressed periods associated with the monsoon and MJO circulations. The active monsoon period was characterized by strong upward motion and large advective cooling and moistening through the entire troposphere, while the suppressed and clear periods exhibited moderate midlevel subsidence and significant
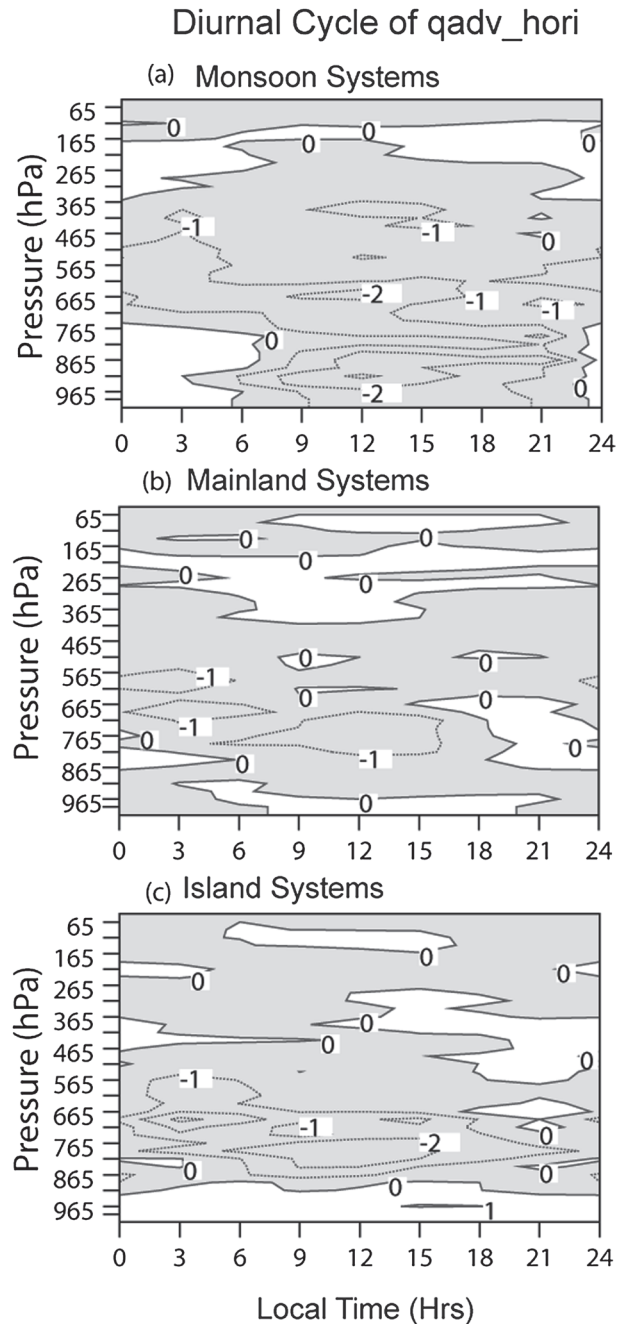
low- to midlevel drying through horizontal advection. The midlevel subsidence and horizontal dry advection contributed to the considerably dryer midtroposphere observed during this period and are likely factors that limit the growth of clouds. During the break period, mean upward motion was accompanied by advective
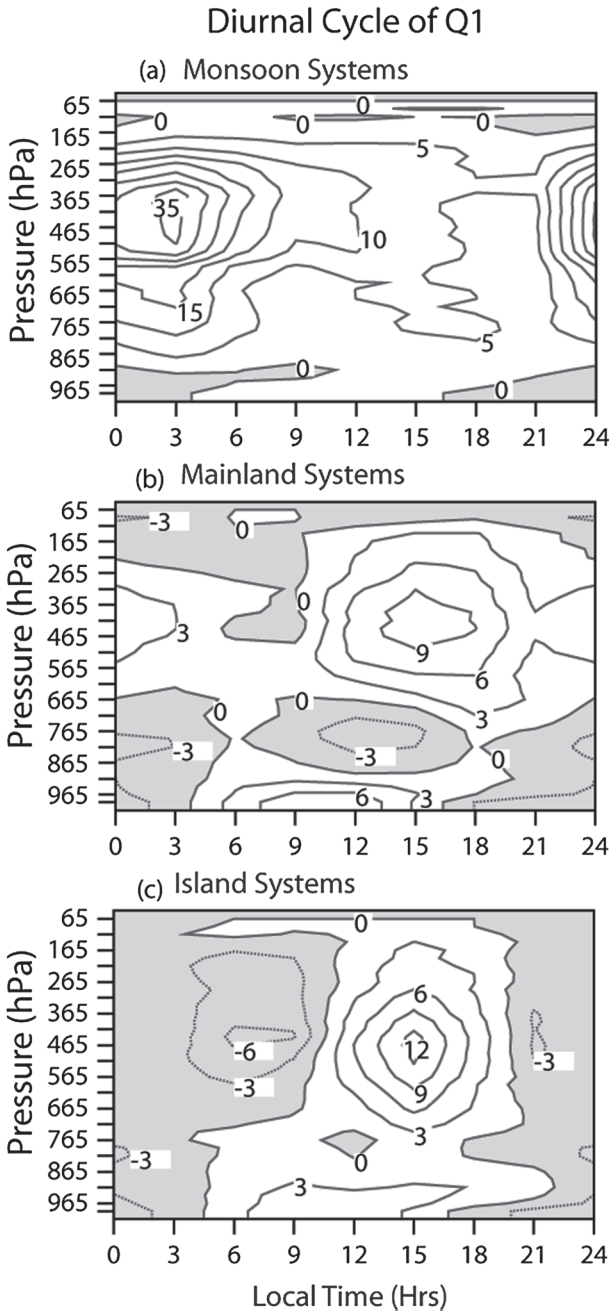
Diurnal Cycle of Q1

(a) Monsoon Systems

(b) Mainland Systems

(c) Island Systems

Local Time (Hrs)

FIG. 18. Diurnal cycle of diabatic heating rates (K day^{-1}). (a) Monsoon systems, (b) mainland systems, and (c) island systems. In (a)–(c), negative values are shaded. Contour interval is 5 in (a) and 3 in (b) and (c).

Diurnal Cycle of Q2

(a) Monsoon Systems

(b) Mainland Systems

(c) Island Systems

Local Time (Hrs)

FIG. 19. Diurnal cycle of diabatic drying rates (K day^{-1}). (a) Monsoon systems, (b) mainland systems, and (c) island systems. In (a)–(c), negative values are shaded. Contour interval is 5 in (a) and 3 in (b) and (c).

cooling and moistening located at midlevels with weak advective warming and drying at low levels. These different large-scale structures are likely important in the interaction of the large-scale environment with tropical convection.

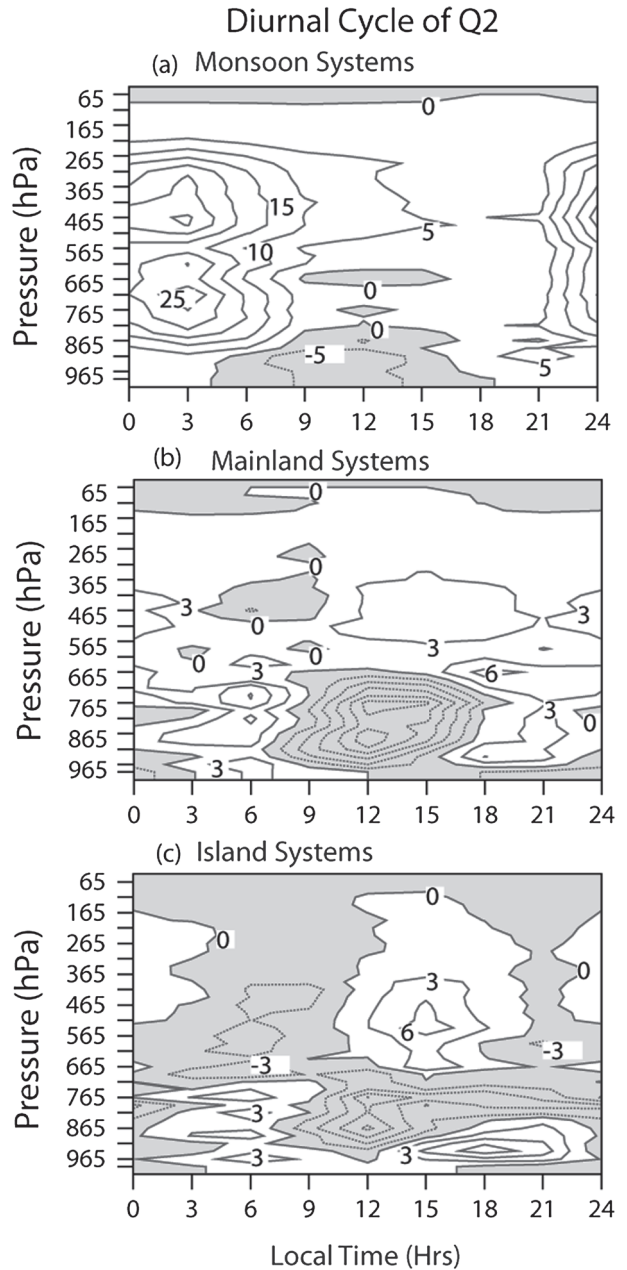The Q1 and Q2 profiles demonstrated considerable variations with different regimes. This appears to result

from differences in the large-scale structures, cloud types, and rainfall rates between the regimes. This is consistent with Schumacher et al. (2007), who showed that large-scale flow variations, surface precipitation rates, and cloud types all played an important role in determining the Q1 profiles based on the data from the KWAJEX, TRMM–LBA, and SCSMEX field campaigns. This study shows that the strongest diabatic heating and drying

occurred during the active monsoon period when the rainfall rates were the largest. In this period, the heating was observed throughout the troposphere with maxima between 350 and 550 hPa, while the drying exhibited a distinct double-peak structure that is presumably associated with cumulus updrafts at low levels and mesoscale updrafts at high levels. These features are similar to those diagnosed from other tropical field campaigns. In contrast, the heating and drying were moderate and only appeared above 700 hPa during the break period. For the suppressed periods, the heating and drying tended to have their maxima at low levels, corresponding to the prevalence of shallow cumulus clouds during these periods.

To further investigate the observed large-scale structure and diabatic heating and drying profiles, a composite analysis has been performed to study the diurnal cycle of the monsoon systems during the active period and the mainland and island convective systems during the break period by using the unique TWP-ICE 3-h sounding data. To more appropriately describe the mainland and island systems, we have performed additional analyses over two subdomains covering the mainland and Tiwi Islands regions.

These systems exhibited significant differences in the large-scale structures and Q1 and Q2 profiles through their diurnal evolutions. Convection during the monsoon period was weak during the day, increased rapidly in the evening, and reached its maximum intensity in the early morning hours. Convection over the mainland and Tiwi Islands domains was initiated primarily by the sea-breeze circulation and confined in the lower troposphere in the midmorning and then quickly developed into deep convection and reached its maximum intensity in the afternoon. The transition from shallow to deep convection is clearly shown in both cloud and Q1 profiles of the mainland and island systems. This is supported by the differences in the large-scale structures between the monsoon systems and the mainland and island systems. The monsoon systems featured upward motion throughout the day with the maximum ascending level in the upper troposphere at 0300 LST because of the nocturnal deep convection. In contrast, the mainland and island systems showed an afternoon maximum in vertical velocity in the mid–upper troposphere. At their initial system development stages (around 0900–1000 LST), the mainland and island systems developed in an environment with an ascending layer near the surface because of the sea breeze circulation and a subsidence layer above, especially for the island systems. The subsidence layer contributes to limiting the mainland and island convective systems to low levels at their initial stages and to focusing convection along sea-breeze convergence lines later in the day.

Although the mainland and island convective systems were both driven by sea breezes, considerable differences were found in their large-scale structures and diabatic heating and drying profiles. We have shown that the island systems had a deeper layer of upward motion and stronger advective moistening near the surface than the mainland systems during the day, which resulted in a deeper low-level diabatic heating and stronger drying in the island systems than the mainland systems. It is also shown that the diurnal cycle of the mainland system was largely influenced by squall lines that passed over the experimental domain at night, which led to the secondary peak in its surface precipitation, large-scale structures, and diabatic heating and drying profiles.

It should be noted that the results shown in this study are based on a relatively small data sample and should be viewed with a degree of caution. Nevertheless, the large-scale structures and diabatic heating and drying profiles revealed in the examined convective systems generally agree with those diagnosed from other tropical field campaigns. Furthermore, the high-frequency (3 hourly) sounding data from TWP-ICE enabled us to perform a diurnal analysis of the convective systems under different surface boundary conditions. This is especially valuable for the mainland and island systems during the break monsoon period since these systems often occur on a daily basis and have much shorter lifetimes than the monsoon systems. By using the intensive sounding measurements combined with other unique observations from the enhanced surface observational network and satellite data, this study has provided a comprehensive description of the large-scale environment and diabatic heating and drying profiles of the tropical convective systems observed during TWP-ICE. It therefore provides important information for future studies on TWP-ICE.

TABLE A1. Empirical RS92 calibration factors $[C_{cal}(T)]$ and their uncertainties derived from nighttime soundings. Reproduced from Vömel et al. (2007).

Temperature (T, Celsius)	$C_{cal}(T)$	Uncertainty
0	0.98	±0.02
−30	0.98	±0.06
−50	0.94	±0.03
−60	1.04	±0.06
−70	1.13	±0.06

APPENDIX

Correction of the Vaisala RS92 Sondes

a. Vömel et al. (2007) method

The Vaisala RS92 sondes are known to have a significant daytime solar radiation dry bias and a minor temperature-dependent calibration error. Vömel et al. (2007) developed an empirical method to correct the bias based on results from a comparison of RS92 humidity observations with reference measurements made by a cryogenic frostpoint hygrometer (CFH). As described in Vömel et al. (2007), the RS92 measured relative humidity can be corrected by using a pressure- (P) dependent radiation error correction factor $C_{rad}(P)$ and a temperature- (T) dependent calibration factor $C_{cal}(T)$. The correction factor can be written as

$$C_{rh} = \frac{RH_{corr}}{RH_{TL}} = \frac{1}{[C_{rad}(P)][C_{cal}(T)]}, \qquad (A1)$$

where RH_{corr} is the corrected relative humidity, RH_{TL} is the time lag corrected humidity profile described by Miloshevich et al. (2004), $C_{cal}(T)$ is given in Table A1, and $C_{rad}(P)$ can be expressed as

$$C_{rad}(P) = -0.12\,158\,\ln(P)^2 + 1.664\,\ln(P) - 4.7855. \qquad (A2)$$

b. Revised Vömel et al. (2007) method for TWP-ICE

The Vömel et al. (2007) method was developed for correcting RS92 soundings launched near solar noon and at night because there were no early morning or late afternoon soundings available over the period they studied. Using the 3-hourly high-frequency TWP-ICE soundings and the ARM microwave radiometer (MWR) measured precipitable water vapor (PWV) from the ship, we found that the dry bias is also dependent on the solar zenith angle with greater bias found for radiosondes launched near solar noon than those made in the early morning or late afternoon. Therefore, the use of the near-noon relative humidity correction factors for early morning or late afternoon soundings is going to result in an overcorrection of the relative humidity. To take into account of this, a new correction factor C_{zen} is introduced into Eq. (A1):

$$C_{rh} = \frac{RH_{corr}}{RH_{TL}} = \frac{C_{zen}}{[C_{rad}(P)][C_{cal}(T)]}, \qquad (A3)$$

where C_{zen} is a function of the zenith angle, z:

$$C_{zen} = 1 + [\min(z, 90)]\left(\frac{C_{rad} - 1}{90}\right). \qquad (A4)$$

The zenith angle correction factor ensures that C_{rh} decreases linearly, from a maximum at local noon to a minimum at nighttime. At noon, RH_{corr} is the same as the daytime correction described in Vömel et al. (2007).

Table A2 shows the biases for soundings made from the ship with various corrections applied. The first column shows the biases for uncorrected soundings, the second column is for soundings corrected using the method described in Vömel et al. (2007), the third column is for soundings corrected using Eqs. (A3) and (A4), and the last column shows the number of soundings that were used in the validation. Results are shown for near-noon soundings ($z < 30°$, first row), all daytime soundings (second row), and all nighttime soundings (last row).

At the ship, the uncorrected soundings show a significant daytime dry bias. When the temperature calibration and pressure-dependent radiation correction are applied, the dry bias is overcorrected, resulting in quite a large moist bias. As discussed above, this is expected because the bias correction method developed by Vömel et al. (2007) was based on soundings made near noon, whereas many of the soundings in this study were for the early morning or late afternoon, when the radiation dry bias is less. Finally, when all the corrections are applied, the PWV bias is significantly reduced, even for the near-noon soundings.

TABLE A2. Bias of PWV derived from radiosonde soundings made from the ship.

Sounding	Uncorrected	C_{rad} and C_{cal}	All corrections	No. of soundings
$Z \leq 30$	−4.4	2.1	0.8	22
Day	−2.5	3.9	1.3	51
Night	−0.7	0.3	0.3	38

Of course, the RS92 dry bias will vary from one launch to the next, as a result of local factors such as cloud cover, which are not accounted for by the correction algorithm. Nevertheless, the correction method presented in this paper provides a simple method for significantly reducing the RS92 relative humidity errors.

REFERENCES

Ackerman, T. P., and G. M. Stokes, 2003: The Atmospheric Radiation Measurement Program. *Phys. Today,* **56,** 38–44.

Beringer, J., L. B. Hutley, N. J. Tapper, and L. Cernusak, 2007: Savanna fires and their impact on net ecosystem productivity in North Australia. *Global Change Biol.,* **13,** 990–1004, doi:10.1111/j.1365-2486.2007.01334.x.

Bringi, V. N., G. J. Huang, V. Chandrasekar, and T. D. Keenan, 2001: An areal rainfall estimator using differential propagation phase: Evaluation using a C-band radar and a dense gauge network in the tropics. *J. Atmos. Oceanic Technol.,* **18,** 1810–1818.

——, ——, ——, and E. Gorgucci, 2002: A methodology for estimating the parameters of a gamma raindrop size distribution model from polarimetric radar data: Application to a squall-line event from the TRMM/Brazil campaign. *J. Atmos. Oceanic Technol.,* **19,** 633–645.

——, T. Tang, and V. Chandrasekar, 2004: Evaluation of a new polarimetrically based Z–R relation. *J. Atmos. Oceanic Technol.,* **21,** 612–622.

Carbone, R. E., J. Wilson, T. D. Keenan, and J. M. Hacker, 2000: Tropical island convection in the absence of significant topography. Part I: Life cycle of diurnally forced convection. *Mon. Wea. Rev.,* **128,** 3459–3480.

Clothiaux, E. E., T. P. Ackerman, G. G. Mace, K. P. Moran, R. T. Marchand, M. Miller, and B. E. Martner, 2000: Objective determination of cloud heights and radar reflectivities using a combination of active remote sensors at the ARM CART sites. *J. Appl. Meteor.,* **39,** 645–665.

Cressman, G. P., 1959: An operational objective analysis scheme. *Mon. Wea. Rev.,* **87,** 367–374.

Frank, W. M., 1978: The life cycle of GATE convective systems. *J. Atmos. Sci.,* **35,** 1256–1264.

——, and J. L. McBride, 1989: The vertical distribution of heating in AMEX and GATE cloud clusters. *J. Atmos. Sci.,* **46,** 3464–3478.

Gunn, B. W., J. L. McBride, G. J. Holland, T. D. Keenan, N. E. Davidson, and H. H. Hendon, 1989: The Australian summer monsoon circulation during AMEX Phase II. *Mon. Wea. Rev.,* **117,** 2554–2574.

Hume, T., 2007: Radiation dry bias in the TWP-ICE radiosonde soundings. *Proc. 17th ARM Science Team Meeting,* Monterey, CA, U.S. Department of Energy, P00011. [Available online at http://www.arm.gov/publications/proceedings/conf17/poster/P00011.pdf.]

Johnson, R. H., 1984: Partitioning tropical heat and moisture budgets into cumulus and mesoscale components: Implications for cumulus parameterization. *Mon. Wea. Rev.,* **112,** 1590–1601.

Keenan, T. D., and R. E. Carbone, 1992: A preliminary morphology of precipitation systems in tropical northern Australia. *Quart. J. Roy. Meteor. Soc.,* **118,** 283–326.

——, and Coauthors, 2000: The Maritime Continent Thunderstorm Experiment (MCTEX): Overview and some results. *Bull. Amer. Meteor. Soc.,* **81,** 2433–2455.

Lin, J., B. Mapes, M. Zhang, and M. Newman, 2004: Stratiform precipitation, vertical heating profiles, and Madden–Julian oscillation. *J. Atmos. Sci.,* **61,** 296–309.

Lin, X., and R. H. Johnson, 1996a: Kinematic and thermodynamic characteristics of the flow over the western Pacific warm pool during TOGA COARE. *J. Atmos. Sci.,* **53,** 695–715.

——, and ——, 1996b: Heating, moistening, and rainfall over the western Pacific warm pool during TOGA COARE. *J. Atmos. Sci.,* **53,** 3367–3383.

Long, C. N., 2001: The shortwave (SW) clear-sky detection and fitting algorithm: Algorithm operational details and explanations. Atmospheric Radiation Measurement Program Tech. Rep. ARM TR-004, 26 pp. [Available online at http://www.arm.gov/publications/tech_reports/arm-tr-004-1.pdf.]

——, and T. P. Ackerman, 2000: Identification of clear skies from broadband pyranometer measurements and calculation of downwelling shortwave cloud effects. *J. Geophys. Res.,* **105D,** 15 609–15 626.

Manton, M. J., and J. L. McBride, 1992: Recent research on the Australian monsoon. *J. Meteor. Soc. Japan,* **70,** 275–285.

May, P. T., J. H. Mather, G. Vaughan, C. Jakob, G. M. McFarquhar, K. N. Brown, and G. G. Mace, 2008: The Tropical Warm Pool International Cloud Experiment. *Bull. Amer. Meteor. Soc.,* **89,** 629–645.

McBride, J. L., 1987: The Australian summer monsoon. *Monsoon Meteorology,* C. P. Chang and T. N. Krishnamurti, Eds., Oxford University Press, 203–231.

Miloshevich, L. M., A. Paukkunen, H. Vömel, and S. J. Oltmans, 2004: Development and validation of a time-lag correction for Vaisala radiosonde humidity measurements. *J. Atmos. Oceanic Technol.,* **21,** 1305–1327.

Minnis, P., and Coauthors, 2001: A near-real-time method for deriving cloud and radiation properties from satellites for weather and climate studies. *Proc. 11th Conf. on Satellite Meteorology and Oceanography,* Madison, WI, Amer. Meteor. Soc., 477–480.

Nesbitt, S. W., and E. J. Zipser, 2003: The diurnal cycle of rainfall and convective intensity according to three years of TRMM measurements. *J. Climate,* **16,** 1456–1475.

Numaguti, A., R. Oki, K. Nakamura, K. Tsuboki, N. Misawa, T. Asai, and Y.-M. Kodama, 1995: 4–5-day-period variation and low-level dry air observed in the equatorial western Pacific during the TOGA-COARE IOP. *J. Meteor. Soc. Japan,* **73,** 267–290.

Riehl, H., and J. S. Malkus, 1958: On the heat balance in the equatorial trough zone. *Geophysica,* **6,** 503–538.

Schumacher, C., M. H. Zhang, and P. E. Ciesielski, 2007: Heating structures of the TRMM field campaigns. *J. Atmos. Sci.,* **64,** 2593–2610.

Simpson, J., T. Keenan, B. R. H. Simpson, and G. J. Holland, 1993: Cumulus mergers in the maritime continent region. *Meteor. Atmos. Phys.,* **51,** 73–99.

Stokes, G. M., and S. E. Schwartz, 1994: The Atmospheric Radiation Measurement (ARM) Program: Programmatic background and design of the cloud and radiation test bed. *Bull. Amer. Meteor. Soc.,* **75,** 1201–1221.

Tao, W.-K., and Coauthors, 2006: Retrieval of latent heating from TRMM measurements. *Bull. Amer. Meteor. Soc.,* **87,** 1555–1572.

——, R. J. Houze, and E. A. Smith, 2007: The fourth TRMM latent heating workshop. *Bull. Amer. Meteor. Soc.,* **88,** 1255–1259.

Thompson, R. M., S. W. Payne, E. E. Recker, and R. J. Reed, 1979: Structure and properties of synoptic-scale wave disturbances in the intertropical convergence zone of the eastern Atlantic. *J. Atmos. Sci.,* **36,** 53–72.

Vömel, H., and Coauthors, 2007: Radiation dry bias of the Vaisala RS 92 humidity sensor. *J. Atmos. Oceanic Technol.,* **24,** 953–963.

Xie, S., S. A. Klein, M. Zhang, J. J. Yio, R. T. Cederwall, and R. McCoy, 2006: Developing large-scale forcing data for single-column and cloud-resolving models from the Mixed-Phase Arctic Cloud Experiment. *J. Geophys. Res.,* **111,** D19104, doi:10.1029/2005JD006950.

Yanai, M., 1961: A detailed analysis of typhoon formation. *J. Meteor. Soc. Japan,* **39,** 187–214.

——, and R. Johnson, 1993: Impacts of cumulus convection on thermodynamic fields. *The Representation of Cumulus Convection in Numerical Models, Meteor. Monogr.,* No. 46, Amer. Meteor. Soc., 39–62.

——, S. Esbensen, and J. Chu, 1973: Determination of bulk properties of tropical cloud clusters from large-scale heat and moisture budgets. *J. Atmos. Sci.,* **30,** 611–627.

——, B. Chen, and W.-W. Tung, 2000: The Madden–Julian oscillation observed during the TOGA COARE IOP: Global view. *J. Atmos. Sci.,* **57,** 2374–2396.

Zhang, M. H., and J. L. Lin, 1997: Constrained variational analysis of sounding data bases on column-integrated budgets of mass, heat, moisture, and momentum: Approach and application to ARM measurements. *J. Atmos. Sci.,* **54,** 1503–1524.

——, ——, R. T. Cederwall, J. J. Yio, and S. C. Xie, 2001: Objective analysis of ARM IOP data: Method and sensitivity. *Mon. Wea. Rev.,* **129,** 295–311.